International Journal of Fatigue 162 (2022) 106946

Contents lists available at ScienceDirect

International Journal of Fatigue

journal homepage: www.elsevier.com/locate/ijfatigue

Fatigue properties and S-N curve estimating of 316L stainless steel prepared by SLM

Fanyu Zeng [a], Yongtai Yang [a,b,*], Guian Qian [b,c]

[a] Quanzhou Institute of Equipment Manufacturing, Fujian Institute of Research on the Structure of Matter, Chinese Academy of Science, Jinjiang 362200, Fujian Province, China
[b] University of Chinese Academy of Sciences, Beijing 100049, China
[c] State Key Laboratory of Nonlinear Mechanics (LNM), Institute of Mechanics, Chinese Academy of Sciences, Beijing 100190, China

ARTICLE INFO

Keywords:
Metal additive manufacturing
316L stainless steel
DMS-PSO
Fatigue performance
S-N curve

ABSTRACT

This paper investigates the fatigue properties of 316L stainless steel manufactured by selective laser melting technology (SLM) under hot-isostatic-pressing (HIP) heat-treatment. The fatigue tests of 316L specimens were carried out under pulse tensile cyclic loading to obtain the fatigue performance. To avoid falling into local optima and improve the convergence speed, the dynamic multiswarm particle swarm optimizer (DMS-PSO) algorithm was first introduced for parameter optimization of the three-parameter Weibull distribution model, and then the S-N curves based on the model were obtained. The S-N curves were highly consistent with the metallographic and fractographic phenomena. Besides, both the S-N curves and fractographic analysis show that the resistance of high-stress fatigue fracture is significantly improved by using HIP heat-treatment.

1. Introduction

1.1. Metal additive manufacturing technology

In the field of shoe mold, the application of metal additive manufacturing (AM) technology made integration of shoe design, replacing the traditional mold casting, which made the previously lengthy production process much faster. AM technology produces metallic components by dividing the digital model into different layers through the computer and printing entity model layer by layer. The development of metal additive manufacturing technology has brought new possibilities to the manufacturing industry and created a new industrial production model that combines integrated design and fast manufacturing. Selective laser melting technology (SLM) is the most representative additive manufacturing technology based on the principle of powder spreading. It is a manufacturing method that uses high-temperature lasers for melting and shaping the powder from bottom to top, then the metal parts of high-density and precise are produced by all the layers overlay [1,2]. In this way, freedom of the technical design has risen compared with traditional manufacturing, because powder melting molding improves the utilization efficiency of materials in preparation, and forms specific parts with complex shapes quickly. Consequently, SLM is suitable for the production of aerospace components, precision molds, dies of high-precision, etc. [3,4].

1.2. SLM of 316L

Studies of AM metal parts in recent years focused on three aerospace materials including 316L, Ti6Al4V and AlSi10Mg. For 316L, an ultra-low carbon austenitic stainless steel, the quasi-static mechanical properties were affected by the SLM process parameter strongly, which includes laser energy power, laser scanning speed, scan line spacing, etc. And it has been known that mechanical properties were affected by the laser conditions: high power (HP) laser and low power (LP) laser [5]. Recent research compared the properties of SLM316L and conventionally manufactured (CM) 316L under different scanning strategies [6]. For example, the greater scan line spacing comes the greater the surface roughness [7]. However, the appropriate parameters of SLM should not only achieve great mechanical properties but also improve the density. Part porosity and material connection have been observed by a nondestructive test method (XCT) and traditional metallographic cross-sectional analysis [8]. There were inevitable defects in SLM production, such as metal warping and incomplete melting zone after rapid condensation. Therefore, different post-processes were applied to reduce the residual stress and surface roughness [9]. As an efficient way to improve hardness, post heat treatment has been the first choice of most factories. In addition, the mechanical structure and corrosion resistance

* Corresponding author.
E-mail address: yangyongtai@fjirsm.ac.cn (Y. Yang).

https://doi.org/10.1016/j.ijfatigue.2022.106946
Received 14 January 2022; Received in revised form 4 April 2022; Accepted 20 April 2022
Available online 25 April 2022

Nomenclature

v	Laser scanning speed
s	Scan line spacing
e	Thickness of the powder layer
P	Laser energy power
Ψ	Energy density
σ_m	Mean stress
σ_a, S_a	Stress amplitude
$\sigma_{\max}$	Maximum stress
a_0	Constant term in a S–N curve equation
a_1	Scale coefficient in a S–N curve equation
β	Shape parameter of the Weibull distribution
η	Scale parameter of the Weibull distribution
$f(x)$	Probability density function
$F(x)$	Cumulative density function
δ_i	Characteristic parameter
y	Fracture probability
ε	Accuracy of termination condition
pBest	Historical optimal position of each particle
gBest	Global optimal position of the whole particle swarm
sgBest	Global optimal value of each sub-particle swarm
v_{id}^k	Velocity of particle i in the k-th iteration
x_{id}^k	Position of particle i in the k-th iteration
ω	Inertia weight coefficient
c_1	Local learning factor
c_2	Global learning factor
r_1, r_2	Random number
k	Number of iterations
$Nc_{\max}$	Maximum number of iterations
m	Population number

Acronyms

SLM	Selective laser melting
AM	Additive manufacturing
HIP	Hot-isostatic-pressing heat-treatment
DASA	Differential ant-stigmergy algorithm
PSO	Particle swarm optimization
DMS-PSO	Dynamic multiswarm particle swarm optimizer
HP	High power laser
LP	Low power laser
CM	Conventionally manufactured
XCT	X-band communications Transponder
MLE	Maximum likelihood estimation cost function
EDS	Energy dispersive X-ray spectroscopic observation

of AM materials were not related to the temperature of post heat treatment linearly [10], which are reflected by the microstructure after heat treatment [11].

For fatigue properties, laminated defects such as porosity in AM materials lead to increased experimental discreteness and premature failure. Although SLM 316L exhibits higher strength with finer microstructure than CM316L, deteriorated fatigue properties caused by defects and rough surfaces occur in many instances [6]. Polishing can ameliorate this fatigue behavior, but it is difficult to implement for a specific structure. Hot-isostatic-pressing (HIP) heat treatment is beneficial to homogenize the surface morphology and crystal structure, thereby reducing the formation of defects, gas pores, and voids associated with residual stresses. Diverse heat-treated processes affect the fatigue performance of materials directly [12]. Furthermore, research in early times has concluded that the fatigue life of SLM316L is higher than CM316L [13,14]. Therefore, we discussed the effect of HIP treatment at 900°C on SLM316L in this study.

1.3. S-N curve estimating

The fatigue performance of AM materials has not yet been well understood because of their microstructure. Early studies have recognized that structural failure may be caused by cyclic load much lower than its static strength [15,16]. And fatigue damage begins with the propagation of microcracks, which leads to the collapse of the structure. Therefore, the fatigue life prediction can be divided roughly into three categories with different focuses: crack propagation, fatigue damage and S-N curve.

For crack propagation, the interaction among cracks is considered by using two-dimensional or three-dimensional crack solutions to calculate the stress intensity factor of multi-surface cracks, which were verified with the finite element method (FEM) [17]. Fatigue life estimation using FEM has been a good alternative to experimental methods [18,19]. And FEM can predict not only the total fatigue life, but also the crack length in a certain number of load cycles.

For fatigue damage, it is characterized by crack nucleation, coalescence and propagation, which lead to yielding or brittle fracture ultimately [20]. The continuum damage mechanics (CDM) quantify the fatigue damage cumulatively, and predicts the remaining fatigue life (RFL) by computing damage parameters [21]. This prediction method follows the Palmgren-Miner linear damage rule (LDR), which is widely applied owing to its intrinsic simplicity [22,23]. Moreover, other nonlinear theories and thermodynamics-based CDM models have been developed to predict high-cycle fatigue life. Although this method is particularly useful, the rationality of CDM modeling requires long-term and expensive experimental tests. And the differences in specific materials and structures are inevitable because of the different model parameters and plastic deformation mechanism.

For fatigue life, fatigue performance can be represented by the S-N curve which describes a relation between the load cycle and the stress. High-cycle fatigue life of materials was almost estimated by linear regression of S-N curve in double logarithmic scale. In this approach, linear parameters were obtained by the least-square method, and fatigue limits were determined by step-stress method before 10^7 loading cycles. Estimation in this way has proposed a hypothesis that failure data were normally distributed, which was inappropriate in the low probability rupture case [24].

Nowadays, the Basquin model is still applied to analyze the fatigue life of steel structures. However, the model only provides basic geometric descriptions of S-N curves, which do not consider the statistical distribution. In particular, stochastic amounts of defects could increase the scatter of the SLM316L parts [25]. Therefore, a linear model which follows the lognormal or Weibull life distribution is more efficient in life prediction [26]. Moreover, it has been known that the Weibull distribution is the most suitable one for life analysis [27]. The distribution model has been carried out to approximate the S-N curves of many materials [28–30], and the subsequent research made a contrastive analysis between Weibull distribution and experimental data. Klemenc J [31] has proposed a method to simulate probability density in each stress amplitude according to test data. And the distributed scatter was used to evaluate the reliability of materials, while the runouts obtained from the fatigue experiments are also considered in this method. Although there existed a threshold from the left side, and the fatigue limit calculation was an extra part of the approach [32], it still has applied value because of the association with fatigue data in real cases. The parameters of the S-N estimation are calculated by applying the maximum likelihood estimation (MLE) method [33], which requires two geometrical parameters and three parameters of the Weibull distribution as well. To obtain these parameters, the dynamic multiswarm particle

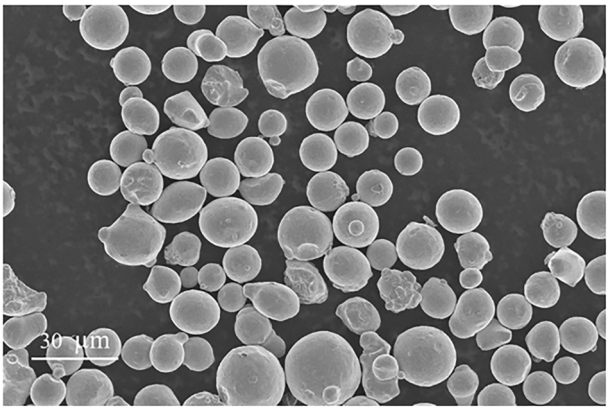

Fig. 1. powder of 316L stainless steel.

swarm optimizer (DMS-PSO) was first applied to minimize negative values of the cost function, which is described specifically in section 4. DMS-PSO algorithm is an evolutionary algorithm with the ability to avoid the local optimum. And DMS-PSO algorithm gives better performance on complex multi-modal problems when compared with the traditional global algorithm [34]. However, the efficiency of fatigue life prediction for AM material based on three-parameter Weibull distribution by DMS-PSO needs to be re-verified, for the specific manufacturing process which affected SLM fatigue properties severely [35]. Then further comparisons are made between the predicted results and experimental data of two real 316L cases under different post-processing. In research [36], fatigue performance of AM AlSi10Mg has been evaluated. Our research presents an application of S-N curve estimating in SLM316L, while detailed parametric studies using DMS-PSO are conducted to investigate the effects of HIP heat-treatment. The results are analyzed and discussed by the fracture metallography.

1.4. Outline of the paper

This study tested 316L stainless steel prepared by SLM. During the preparation of the specimen, a part of them were heat-treated for two hours by hot-isostatic-pressing (HIP) process at 900℃, then air-cooled to room temperature, while others were untreated. After experimental fatigue data were gained by tests, the S-N estimating scatter can be characterized. The specific steps are as follows:

1) Through quasi-static test and fatigue test, the static tensile properties and fatigue data of 316L in two processes were tested respectively;
2) The predicted discrete scatter is obtained by citing the three-parameters Weibull distribution model, and the feasibility of the model is evaluated by comparing the results of the S-N estimating with the test data;
3) Observe the fatigue fracture after fracture and analyze the reasons for the difference in mechanical properties of 316L prepared by SLM.

2. Materials and specimen preparation

2.1. 316L powder

The 316L stainless steel in this study was manufactured by SLM, and the metal powder is shown in Fig. 1. In metal additive manufacturing, the mechanical properties of SLM specimens were relevant to the chemical composition of metal powders. The proportion of rare elements Ni and Mo is an important criterion for the quality of stainless steel. The chemical composition of powders is shown in Table 1. (In 316L, 10%~14% Ni element can improve the strength of the steel and maintain good plasticity; 2%~3% Mo element can refine the steel grains and improve corrosion resistance.) In the test, the fine powder (15 ~ 53 μm) is selected for better strength and hardness, and the microscopic powder particles are almost spherical.

2.2. SLM equipment

The 316L stainless steel specimens were prepared by SLM equipment BLT-S400, which is shown in Fig. 2. In preparation, the laser of this equipment adopted the dual laser beams scanning method (laser power is 2 × 500 W, the maximum output power is 10 kW), while the maximum molding size is 400 mm × 250 mm × 400 mm, and the thickness of the print slice is 0.03 mm. Oxygen is evacuated from the forming cylinder during the preparation process to prevent the residual stress and the warping deformation caused by uneven heating of the specimen, while nitrogen is used for protection to maintain the molten layer condensed by high-pressure extrusion. The relationship of manufacturing parameters is listed as follows:

$$\Psi = \frac{P}{v \cdot e \cdot s} \tag{1}$$

where Ψ is the energy density, P is the laser energy power, v is the laser scanning speed, e is the thickness of the powder layer, and s is the scan line spacing.

In Eq. (1), the energy density Ψ describes the total work of laser output per second and volume, which is directly proportional to the laser energy P and inversely proportional to other parameters [37]. When the energy density Ψ is high, residual stress results from uneven heating. When the energy density Ψ is small, it is easy to produce an incomplete melting region where the powder is not completely melted. Therefore, selecting a suitable energy density has a great impact on the mechanical properties of the material. The density of parts at high-power HP is usually higher than that under low-power LP, and large defects will also

Fig. 2. SLM equipment BLT-S400.

Table 1
Powder material parameters (wt.%).

C	Si	Mn	P	S	Cr	Ni	Mo	O	else
0.012	0.69	1.26	0.010	0.007	16.47	12.72	2.44	0.062	—

Table 2
Equipment technological parameters.

Number	Model	v(mm/s)	s(Mm)	e(Mm)	P(W)	Ψ(J/mm^3)
1	BLT-S400	960	0.1	0.03	245	85.07

decrease with the increase of energy density. However, if the energy density Ψ exceeds a certain critical value, the number of large defects will increase sharply [38]. In addition, the SLM device scans from the edge of the layer to the entire area along the parallel scanning path at a certain angle. The process parameters are shown in Table 2.

For the mechanical test, the static mechanical properties of the material were measured through the quasi-static test at first. Then the fatigue performance of the material was tested based on the quasi-static experimental data. The specimens of the quasi-static test were carried out following the standard GB/T 228.1–2010 [39], as shown in Fig. 3(a). And the fatigue specimens were performed following the standard GB/T 3075–2008 [40], as shown in Fig. 3(b). All specimens were built in vertical orientation, as shown in Fig. 3(c). If the printing plate is defined as the x-y plane of the Cartesian coordinate system, the mechanical property of the z-axis printing is the worst according to the vertical stacking direction of each layer [41]. This study analyzed the direction

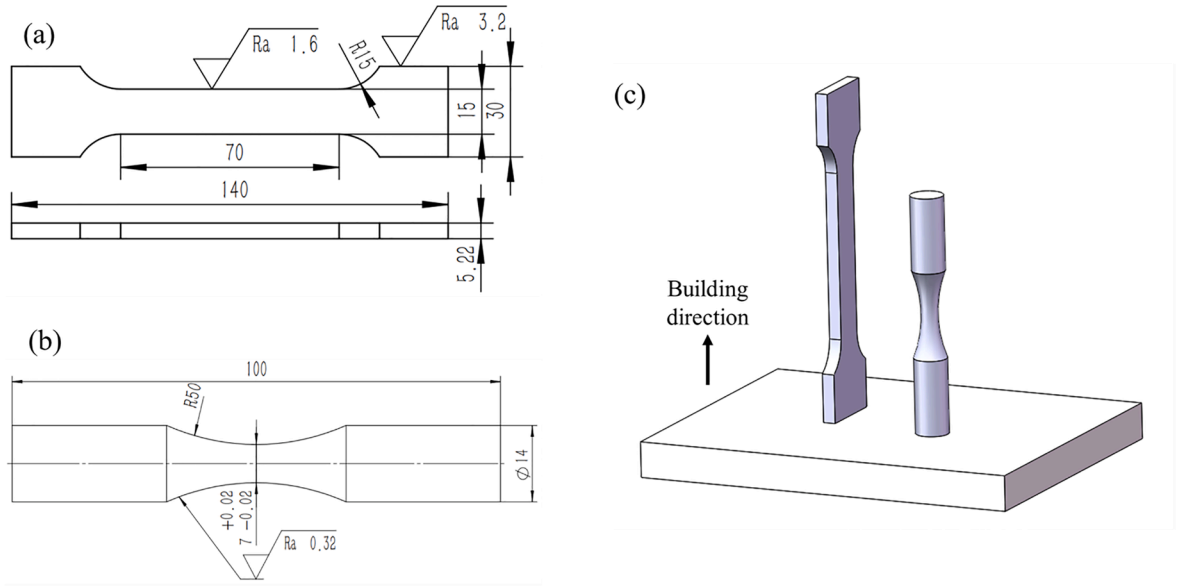

Fig. 3. Specimen size and forming direction: (a) static test specimen; (b) fatigue test specimen; (c) forming direction.

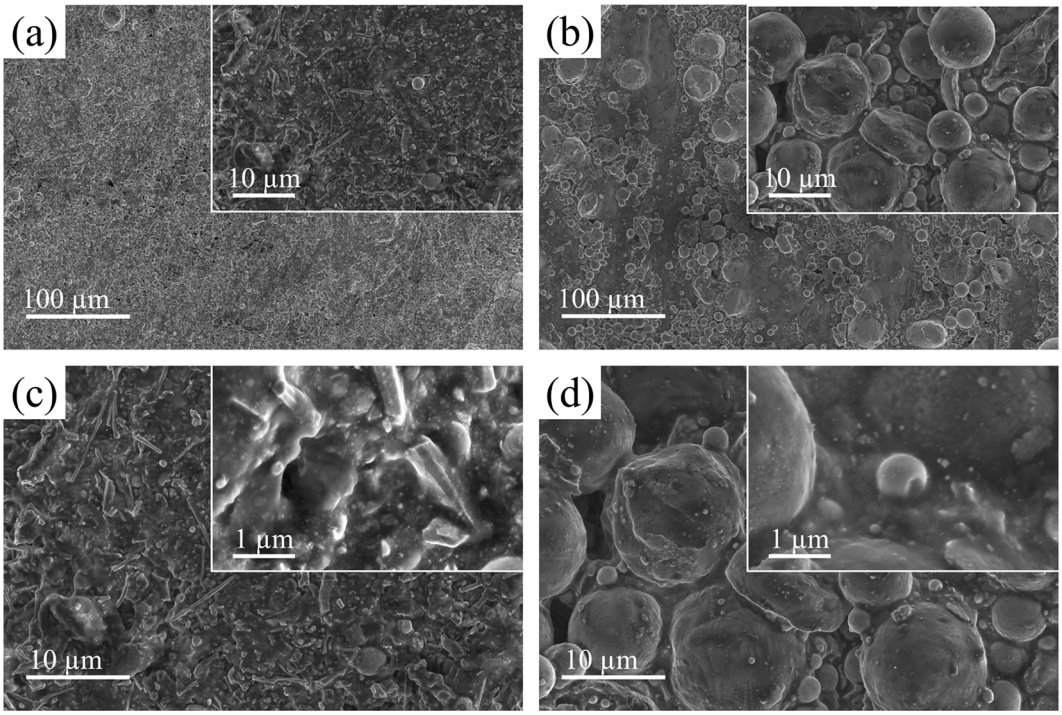

Fig. 4. Microscopic surface topography: (a) Group A surface (10–100 μm); (b) Group B surface (10–100 μm); (c) Group A surface (1–10 μm); (d) Group B surface (1–10 μm).

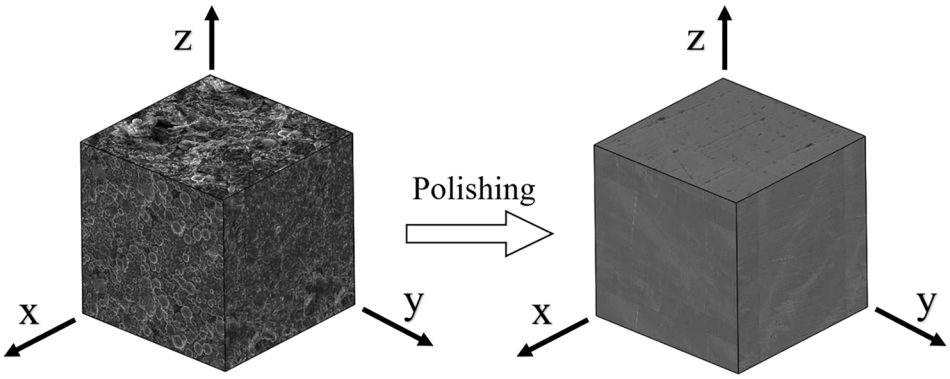

Fig. 5. Surface topography of each surface before and after polishing.

Table 3
Fatigue test plan.

Number	Mean stress σ_m (MPa)	Stress amplitude σ_a (MPa)	Number	Mean stress σ_m (MPa)	Stress amplitude σ_a (MPa)	Number	Mean stress σ_m (MPa)	Stress amplitude σ_a (MPa)
Heat treatment (Group A)								
1	248.72	248.72	9	186.54	186.54	17	124.36	124.36
2	217.63	217.63	10	155.45	155.45	18	248.72	248.72
3	186.54	186.54	11	124.36	124.36	19	217.63	217.63
4	155.45	155.45	12	93.27	93.27	20	186.54	186.54
5	124.36	124.36	13	248.72	248.72	21	155.45	155.45
6[a]	108.82	108.82	14	217.63	217.63	22	124.36	124.36
7	248.72	248.72	15	186.54	186.54	23	93.27	93.27
8	217.63	217.63	16	155.45	155.45			
Not heat-treated (Group B)								
1	245.92	245.92	9	184.44	184.44	17	122.96	122.96
2	215.18	215.18	10	153.70	153.70	18	245.92	245.92
3	184.44	184.44	11	122.96	122.96	19	215.18	215.18
4	153.70	153.70	12	92.22	92.22	20	184.44	184.44
5	122.96	122.96	13	245.92	245.92	21	153.70	153.70
6[a]	107.59	107.59	14	215.18	215.18	22	122.96	122.96
7	245.92	245.92	15	184.44	184.44	23	92.22	92.22
8	215.18	215.18	16	153.70	153.70			

[a] is the data used to validate the model.

of low strength in 316L by SLM. The grain boundary and region division in the fatigue fracture could be observed clearly in this laser scanning strategy, due to the high ductility of the longitudinally.

2.3. Surface of specimens

Each slice layer of 316L prepared by SLM was formed by melting metal powder using middle power (MP) laser. And the spherical defects caused by spattering appeared in the region where the powder is not completely dissolved. This phenomenon also existed in this study. When the manufacturing parameters were fixed, it was found that there were obvious differences in the surface between the specimens of group A (heat-treated) with those of group B (not heat-treated).

The surface of group B reflects the real surface condition after manufacturing, as shown in Fig. 4(b) and Fig. 4(d). There are unfused regions and spherical defects caused by splashing, which indicates that the laser power and speed are not adjusted properly. According to the surface, each printing layer may have pores that are not completely melted and condensed. However, the defects of the specimens in group A are significantly reduced, as the epitaxial dendrite phase is about 0.3 ~ 0.5 μm. During the recrystallization process, the spatial migration path of the solid–liquid interface is blocked, and the crystal shape is irregular, as shown in Fig. 4(a) and Fig. 4(c). It can be seen that through the heat treatment process, the unfused and spherical defects on the metal surface will be recrystallized and precipitated into dendritic phases. And the gap in the melting region is smaller after heat treatment, indicating that the internal residual stress is released and the overall stability of the metal is improved.

However, the overall surface morphology is rough under this process parameter, while the surface textures have significant negative effects on the fatigue strength. The incompletely melted powder particles on the surface will lead to the formation of a stress concentration area. And particles are potential crack initiation points [42], resulting in reducing the fatigue strength of the specimen [43,44].

Therefore, Specimens necessitate post-treatments to remove defects to ensure the reliability of the metal fatigue performance. In this test, all specimens were polished uniformly, and the original and polished surface roughness were respectively 15.18 μm and 0.5 μm. The surface morphology characteristics of the three directions after polishing are shown in Fig. 5.

3. Test method

3.1. Quasi-static test

All tests were divided into two groups, A and B. Group A was heat-treated (900℃, 2 h) by HIP process, while group B was not heat-treated. The quasi-static tests had four tests in each group: the whole tensile properties were tested in the first to third tests, and the fourth test was only to test the Poisson's ratio by a dynamic strain gauge in the elastic phase. The test equipment is a 300kN MTS universal testing machine with an extensometer, which model is E45.305.

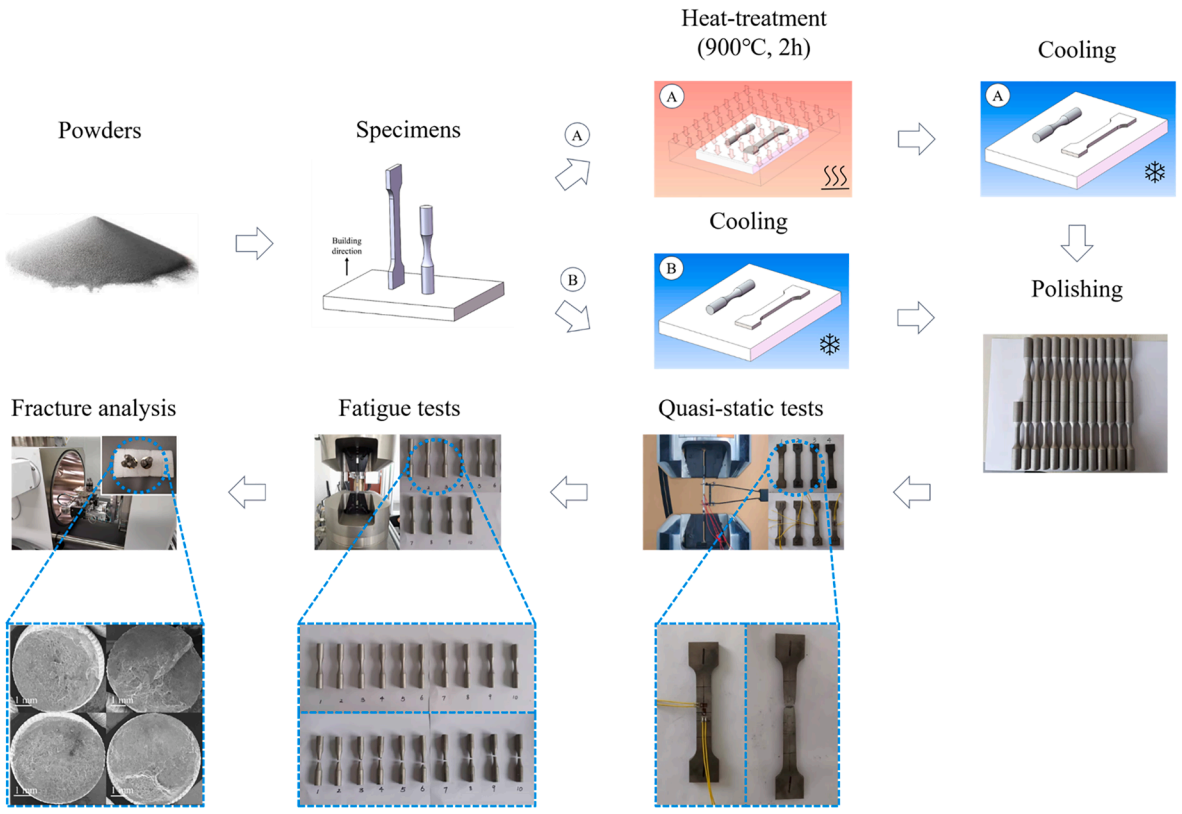

Fig. 6. Test process of SLM 316L.

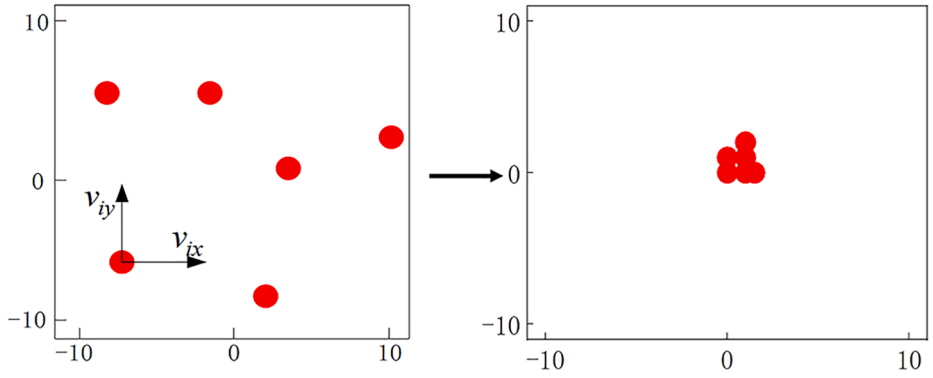

Fig. 7. A schematic view of a two-dimensional PSO optimization.

3.2. Fatigue test

Based on the results of the quasi-static test, the high-cycle fatigue life of specimens was tested using different stress levels to obtain a 316L fatigue life point diagram and a preliminary S-N curve. Four specimens were tested under reducing stress levels, until the loading cycles reached 10^7 times which is regarded as the fatigue limit. The loading frequency f of fatigue testing machine (DST-1105) was set as 30 Hz, while cyclic loading stress ratio ($R = 0$) was the sine wave. The specific load conditions are shown in Table 3:

3.3. Fracture metallography

In metal fatigue rupture, abnormal fracture corresponds to unanticipated fatigue life. Therefore, it is necessary to observe the microstructure of fatigue fracture under each stress level and analyze fatigue data associated with the surface morphology of formed parts. Specifically, a scanning electron microscope (FEI Apreo S) was used to analyze the fatigue fracture, as the Energy dispersive spectroscopy (SU1510) was used to analyze the elements of the fracture.

In summary, the test process of this paper is carried out as shown in Fig. 6.

4. S-N curve model

4.1. High cycle fatigue life model based on MLE

In terms of the S-N curve which illustrates the relation between cyclic load and failure stress, the formula of the classic method to estimate fatigue life in the high-cycle fatigue domain is as follows:

$$\frac{N_1}{N_2} = \left(\frac{S_1}{S_2}\right)^{-k} \tag{4}$$

S_1 and S_2 are two amplitude forces in high cycle fatigue, N_1 and N_2

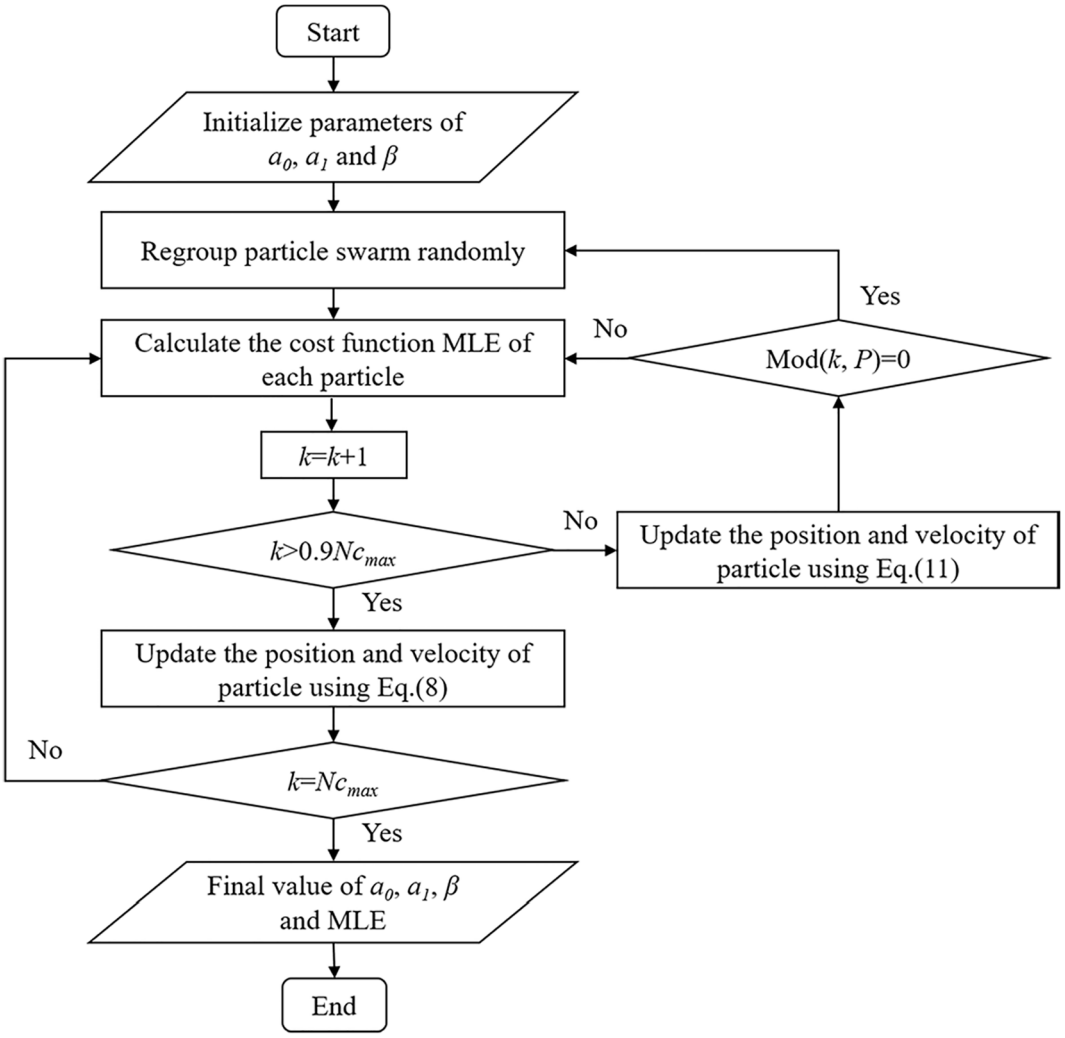

Fig. 8. Optimization process by DMS-PSO.

Table 4
Fatigue test data list of S420MC steel.

S_a(MPa)	N	S_a(MPa)	N	S_a(MPa)	N	S_a(MPa)	N
204	946,200	229	1,555,800	250	389,000	286	175,600
207	1,851,500	229	1,358,000	267	199,400	286	136,500
210	1,281,700	229	1,447,200	267	194,000	295	136,800
211	1,215,000	232	488,400	267	224,800	295	129,900
214	628,100	232	380,500	268	120,800	295	151,400
214	1,307,600	232	567,000	268	139,800	196	2095800[a]
214	1,316,000	232	701,800	268	159,100	196	2176000[a]
214	1,410,600	232	553,000	268	187,100	200	2051500[a]
214	851,900	232	630,000	268	219,600	200	2001300[a]
214	1,566,600	248	286,700	268	238,600	204	2135500[a]
214	959,900	248	376,900	271	259,500	205	2002800[a]
214	1,159,400	248	488,300	271	313,000	205	2003000[a]
219	1,095,800	248	650,100	271	346,100	205	2051500[a]
219	1,499,200	248	585,900	286	61,600	207	2041400[a]
221	1,926,800	248	698,500	286	119,400	211	2168200[a]
224	1,999,500	250	313,700	286	81,600	214	2022700[a]
224	997,600	250	256,900	286	132,000	214	2013300[a]
229	690,600	250	238,800	286	130,000	214	2147000[a]
229	730,500	250	323,500	286	104,300	214	2012500[a]
229	1,009,600	250	213,700	286	97,400		

[a] -Run-outs.

Table 5
Optimization comparison between DMS-PSO and DASA.

S420MC steel	Experimental data		Simulated data
algorithm	DASA	DMS-PSO	DMS-PSO
Number of experimental data points	65	65	500
Requested precision of solution ε	0.0001	0.0001	0.0001
Maximum number of iterations	40,000	40,000	40,000
Optimal solution for parameter a_0	25.6317	25.5065	24.5027
Optimal solution for parameter a_1	−8.3340	−8.2813	−7.8965
Optimal solution for parameter β	2.8163	2.8082	3.9384
Final value of cost function	873.7368	873.7270	6447.9255

are cycles of fatigue rupture under corresponding stress levels, and k is the exponent of the S–N curve. Eq. (4) can be transformed into a linear form by $N_1 = N$ and $S_1 = S$. Early research estimated the S-N curve of many materials in this approach [45],

$$\log(N) = \log(N_2) + k\cdot\log(S_2) - k\cdot\log(S) \tag{5}$$

which is transformed into a Basquin model if:

$$a_0 = \log(N_2) + k\cdot\log(S_2); a_1 = -k$$

In this method, the S-N curve is estimated based on the fatigue life of two different amplitude stress levels in the high cycle fatigue domain. Although this method is easy to implement, it has some obvious disadvantages [31]: Choosing two amplitudes to estimate the probability distribution is a probability hypothesis in itself, which is not suitable for situations with few experimental species. Furthermore, the independent calculation of the probability distribution under each stress level will lead to a relatively large discreteness and illogical failure probability curve. Therefore, the probability density function (PDF) and cumulative density function (CDF) of failure cycles based on different failure probabilities were introduced. For this reason, it was decided to apply the three-parametric Weibull distribution to PDF:

$$f(N/\sigma_{\max}) = \frac{\beta}{\eta(\sigma_{\max})}\cdot\left(\frac{N}{\eta(\sigma_{\max})}\right)^{\beta-1}\cdot\exp\left[-\left(\frac{N}{\eta(\sigma_{\max})}\right)^{\beta}\right] \tag{6}$$

$$\begin{aligned}\eta(\sigma_{\max}) &= 10^{a_0+a_1\log(\sigma_{\max})}; a_0 > 0, a_1 < 0\\ \beta &= const; \beta > 0\\ \sigma_{\max} &= \sigma_a + \sigma_m\end{aligned} \tag{7}$$

where β and η are the shape parameter and scale parameter, σ_a and σ_m are the stress amplitude and mean stress respectively, a_0 and a_1 are the intercept and slope of the Basquin's curve, so the scale parameter η in the equation is not estimated at a single stress level, but is related to all stress levels in the high-cycle fatigue domain. The parameters a_0 and a_1 confirmed by the test data are substituted into the maximum likelihood estimation (MLE) cost function [46], and the parameter with the minimum negative value will be the final result. The MLE cost function is shown in Eq. (8):

$$\begin{aligned}MLE[a_0, a_1, \beta] &= \sum_{i=1}^{n}\{\delta_i\cdot\ln[f(N_i|\sigma_{\max})] + (1-\delta_i)\cdot\ln[1 - F(N_i|\sigma_{\max})]\}\\ \delta_i &= \begin{cases} 1.0, for\ fatigue\ failure \\ 0, for\ run-out\ specimens \end{cases}\\ F(N_i|\sigma_{\max}) &= \int_0^{N_i} f(N_i|\sigma_{\max})dN = 1 - \exp\left[-\left(\frac{N}{\eta(\sigma_{\max})}\right)^{\beta}\right]\end{aligned} \tag{8}$$

where δ_i is the characteristic parameter related to the test, and $F(N_i/\sigma_{\max})$ is the CDF of the Weibull distribution. The maximum likelihood estimation of the equation considers the effect of failure specimens through δ_i. Therefore, the cumulative probability function can be introduced for fatigue analysis when the number of test cycles exceeds the limit.

In this study, the dynamic multiswarm particle swarm optimizer (DMS-PSO) algorithm [47] is applied to minimize the negative value of the cost function, which is compared with the differential ant-stigmergy algorithm (DASA) in the research [48] on astringency. For each

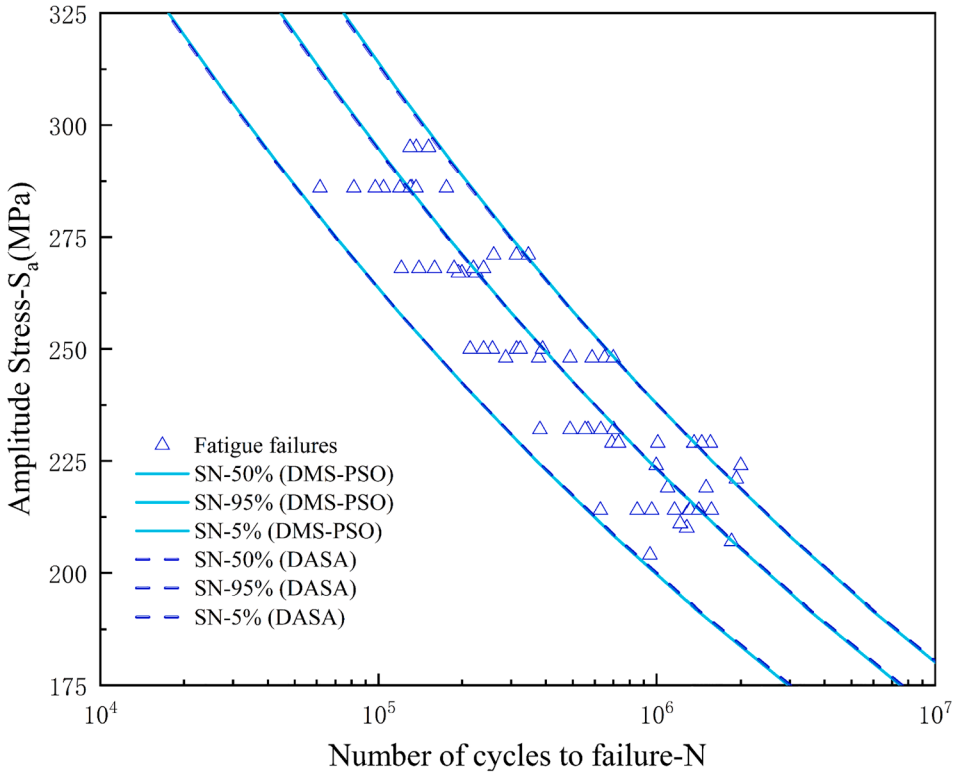

Fig. 9. Estimated scatter of the S–N curves for S420MC.

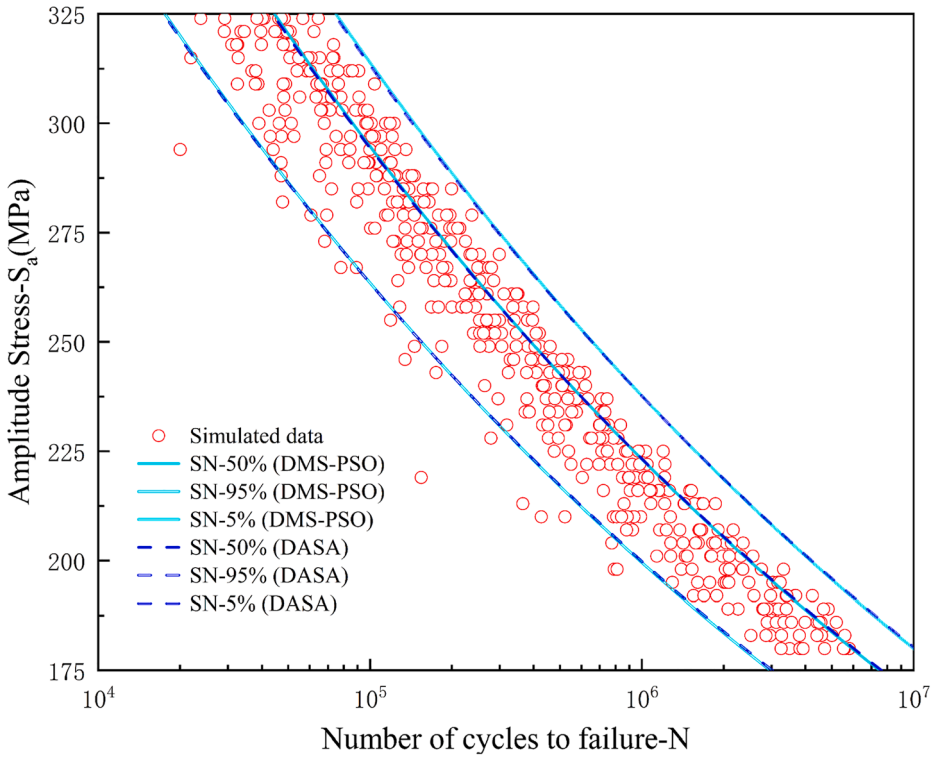

Fig. 10. Estimated scatter of the S–N curves for a simulated sample set with 500 data points.

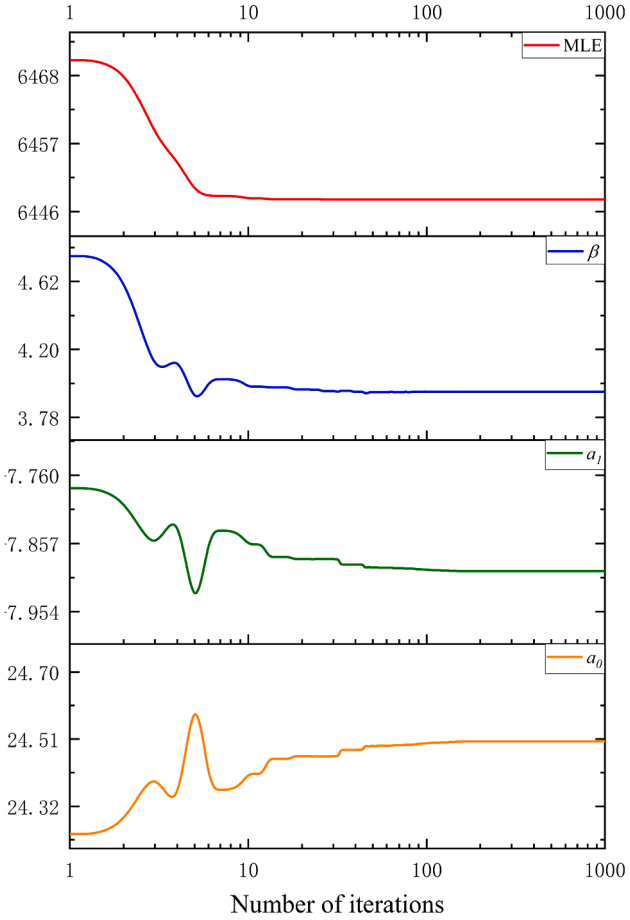

Fig. 11. Iterative convergence of estimation by DMS-PSO.

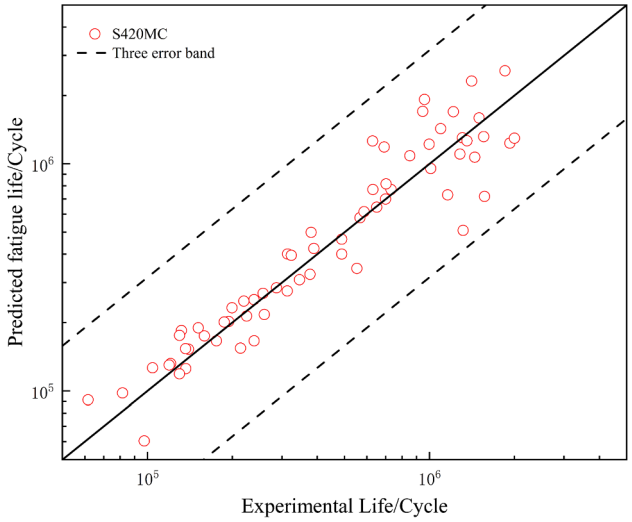

Fig. 12. Variations in the estimated results by the DMS-PSO against the experimental data.

equidistant stress level σ_{max}, separate Weibull distributions of three fracture probabilities (5%, 50% and 95%) will be approximately calculated. In addition, the CDF of any fracture probability y can be built, see Eq. (9):

$$y = F(N_i|\sigma_{max}) = \int_0^{N_i} f(N_i|\sigma_{max})dN = 1 - \exp[-(\frac{N}{\eta(\sigma_{max})})^{\beta}]$$
$$\Rightarrow N_y = N_y(\sigma_{max}) = \eta(\sigma_{max})\cdot[-\ln(1-y)]^{1/\beta} \quad (9)$$

Therefore, the DMS-PSO algorithm necessitates evaluation in the ability of search, specifically in finding the a_0, a_1 and β parameters that minimize the MLE. The optimization is divided into four steps:

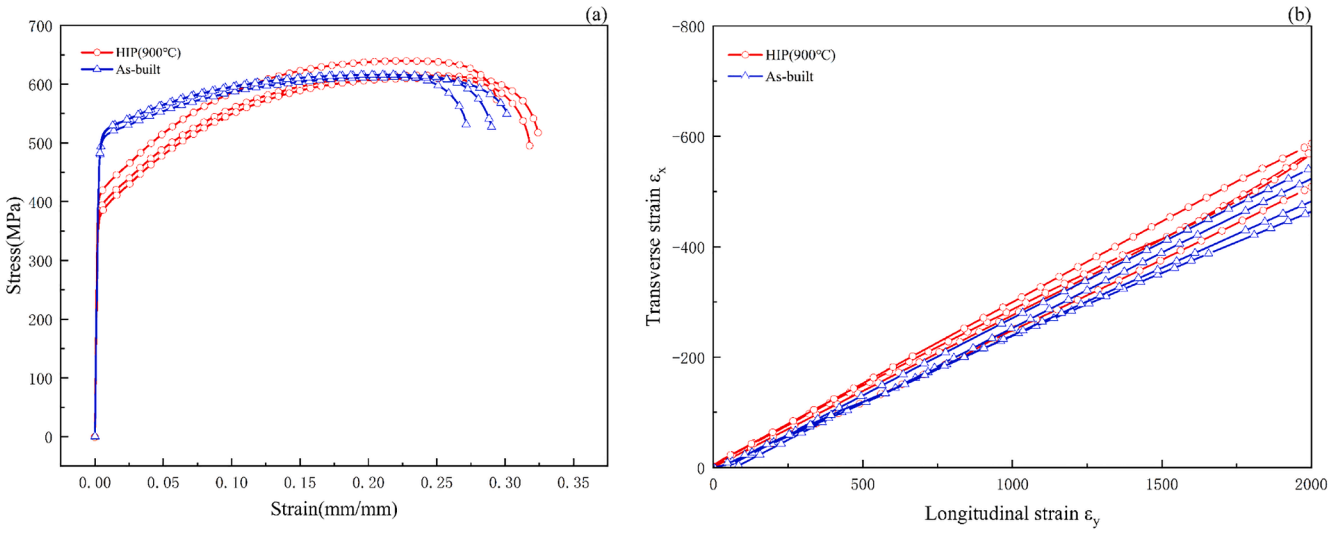

Fig. 13. 316L mechanical properties: (a) stress–strain curve; (b) transverse strain-longitudinal strain curve.

Table 6
Experimental results.

Specimen		Yang's Elastic Modulus (GPa)	Poisson's Ratio	Yield strength (MPa)	Ultimate tensile strength (MPa)	Elongation (%)	Reduction of area (%)
A	1	145.6	0.2720	387.5	615.3	46.90	47.50
	2	140.5	0.2790	377.2	610.2	47.20	50.60
	3	168.2	0.2930	411.8	640.0	46.80	35.00
	4	149.0	0.2560	—	—	—	—
	Average	154.3	0.2750	392.2	621.8	47.97	44.37
	C.V (%)	8.022	5.594	4.530	2.563	0.4432	18.61
B	1	131.8	0.2780	500.1	615.7	41.40	47.20
	2	135.4	0.2700	503.2	616.4	44.80	51.60
	3	138.8	0.2330	496.9	612.2	45.80	43.50
	4	143.6	0.2420	—	—	—	—
	Average	137.4	0.2558	500.1	614.8	44.00	47.43
	C.V (%)	3.657	8.461	0.6399	0.3660	5.2421	8.5489

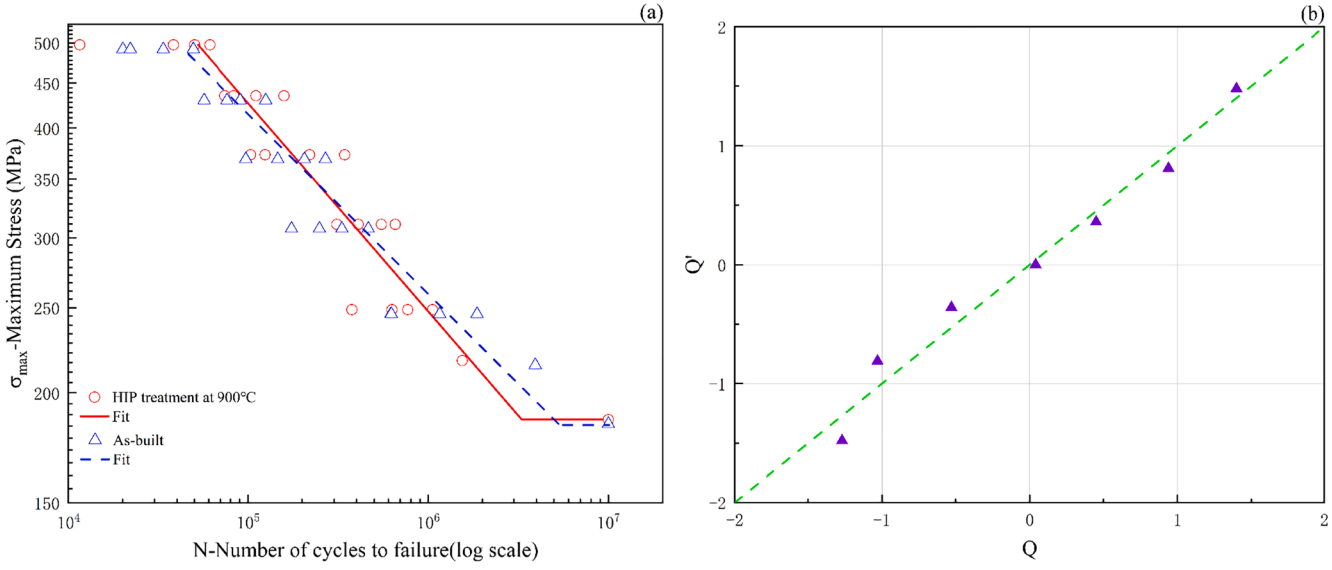

Fig. 14. 316L fatigue performance (R = 0): (a) S-N curve; (b) Q-Q' graph.

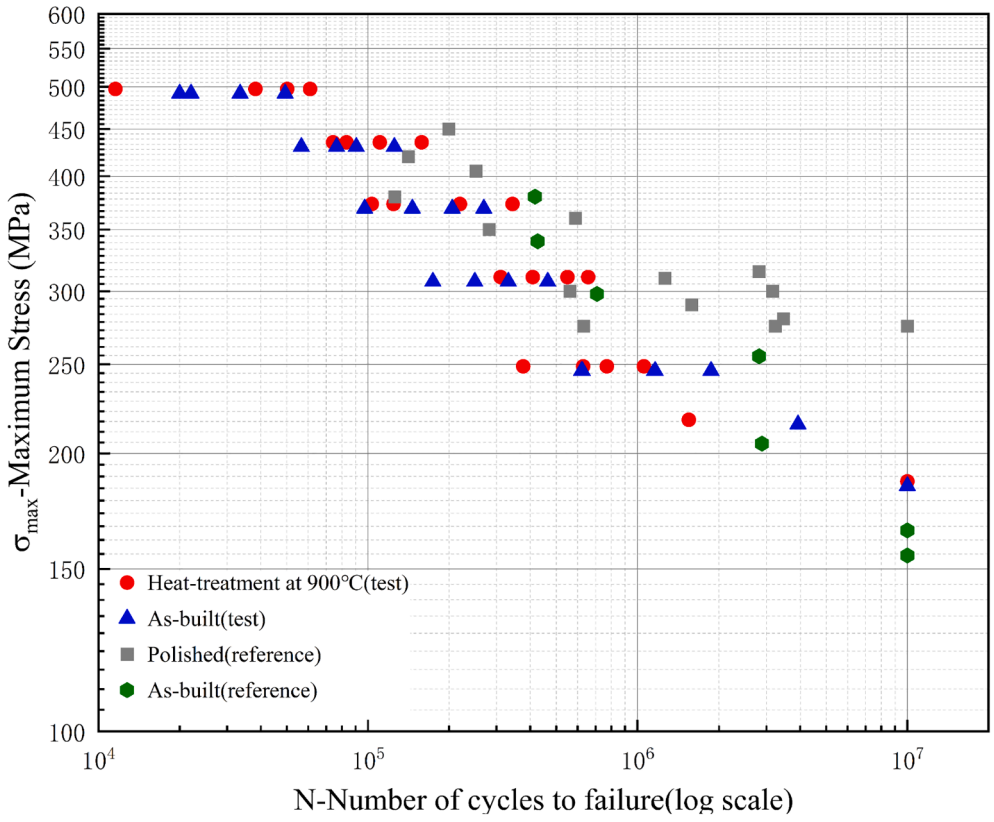

Fig. 15. Fatigue performance of 316L stainless steel under different processes.

Table 7
PSO optimization result (heat treatment, $m = n$).

Number of data points n ($m = n$)	Parameter a_0			Parameter a_1			Parameter β			Cost function (MLE)	
	$a_0^{sr=0}$	Final iteration	difference %	$a_1^{sr=0}$	Final iteration	difference %	$\beta^{sr=0}$	Final iteration	difference %	L_{min}	L_{min}/m
45	17.40	17.05	−2.000	−4.78	−4.61	−3.491	4	4.09	2.189	597.52	13.278
90	17.41	17.19	−1.274	−4.79	−4.67	−2.476	4	3.61	−9.737	1203.10	13.368
180	17.13	17.01	−0.672	−4.66	−4.59	−1.570	4	3.96	−1.118	2401.56	13.342
450	17.14	17.10	−0.214	−4.67	−4.63	−0.863	4	4.01	0.334	5987.39	13.305
900	16.90	16.94	0.208	−4.57	−4.56	−0.241	4	4.02	0.413	11987.03	13.312
1350	16.83	16.91	0.471	−4.54	−4.55	−0.160	4	4.04	0.982	17965.16	13.308

Table 8
PSO optimization result (not heat-treated, $m = n$).

Number of data points n ($m = n$)	Parameter a_0			Parameter a_1			Parameter β			Cost function (MLE)	
	$a_0^{sr=0}$	Final iteration	difference %	$a_1^{sr=0}$	Final iteration	difference %	$\beta^{sr=0}$	Final iteration	difference %	L_{min}	L_{min}/m
45	18.85	18.87	0.066	−5.39	−5.37	−0.433	4	3.40	−15.035	598.57	13.301
90	19.30	19.30	−0.027	−5.57	−5.54	−0.533	4	3.66	−8.568	1193.84	13.265
180	19.12	19.16	0.731	−5.46	−5.49	0.573	4	3.97	−0.696	2372.66	13.181
450	18.99	19.09	0.481	−5.44	−5.46	0.202	4	3.92	−2.024	5950.62	13.224
900	18.99	19.08	0.463	−5.44	−5.45	0.181	4	3.94	−1.479	11911.45	13.235
1350	19.05	19.12	0.342	−5.46	−5.47	0.019	4	4.01	0.139	17840.33	13.215

1) Experimental data points are expanded into a large number of virtual data sets [25], which were used as training sets for DMS-PSO algorithm.
2) The experimental and simulated data set are imported into the DMS-PSO algorithm, to obtain the minimum negative value in MLE cost function iteratively.
3) After optimizing the optimal values of a_0, a_1 and β, the S-N curves and scatters under 5%, 50% and 95% fracture probability were obtained by the three-parameter Weibull distribution model.
4) Finally, the feasibility of the optimization by DMS-PSO algorithm was evaluated by comparison between test data and estimated scatter.

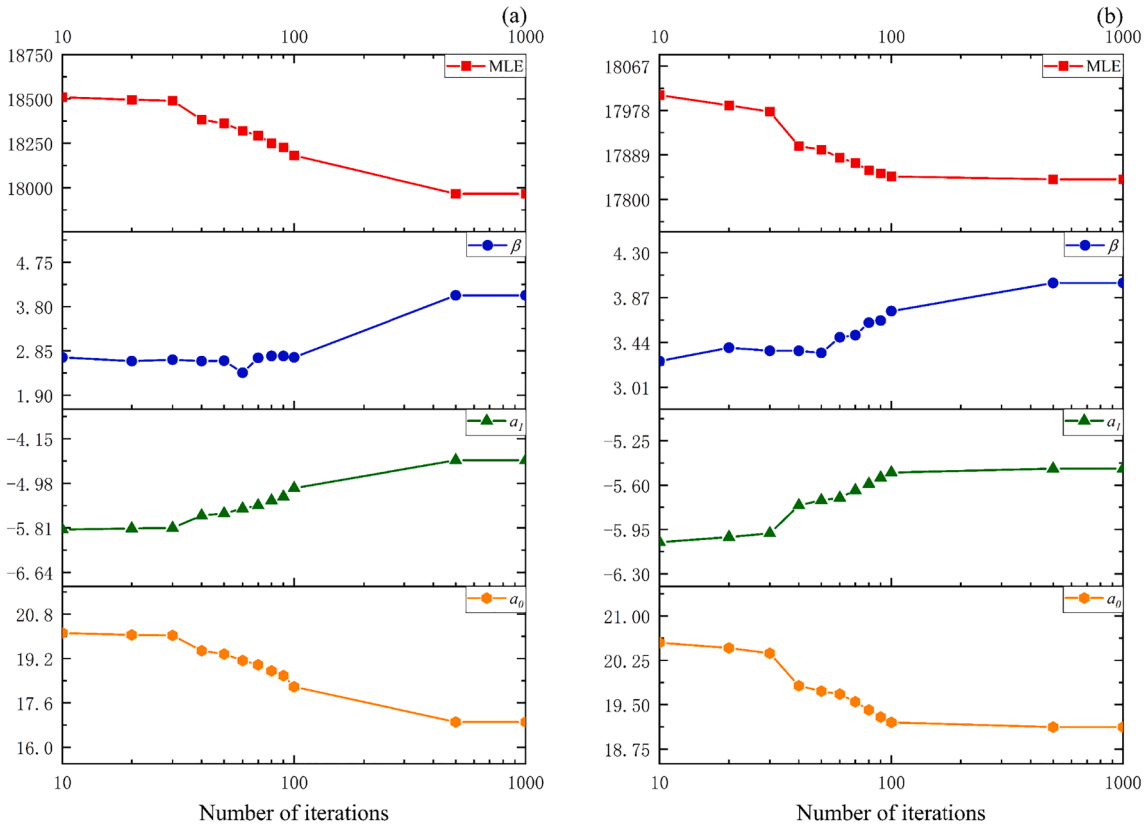

Fig. 16. Variations of optimization iteration value: (a) heat treatment; (b) no heat treatment.

Table 9
Optimization of iteration data and time cost.

iterations	Heat treatment					iterations	Not heat-treated				
	a_0	a_1	β	MLE	time(s)		a_0	a_1	β	MLE	time(s)
0	16.83	−4.54	4		–	0	19.05	−5.46	4		–
10	20.12	−5.84	2.71	18509.60	0.43	10	20.55	−6.05	3.26	18009.07	0.45
20	20.05	−5.82	2.63	18495.66	1.23	20	20.46	−6.01	3.39	17988.26	1.30
30	20.03	−5.81	2.66	18490.12	2.51	30	20.37	−5.98	3.36	17975.71	2.62
40	19.48	−5.58	2.63	18383.35	4.54	40	19.82	−5.76	3.36	17906.48	4.48
50	19.36	−5.54	2.64	18362.46	6.95	50	19.73	−5.72	3.34	17899.89	6.63
60	19.13	−5.45	2.38	18320.02	9.86	60	19.68	−5.70	3.49	17883.72	9.86
70	18.97	−5.39	2.70	18293.88	13.43	70	19.55	−5.64	3.51	17873.01	13.36
80	18.75	−5.30	2.74	18250.77	17.34	80	19.41	−5.59	3.63	17857.98	17.45
90	18.58	−5.23	2.74	18226.59	21.91	90	19.29	−5.54	3.65	17852.17	21.86
100	18.18	−5.07	2.71	18181.87	26.81	100	19.20	−5.50	3.74	17845.87	24.88
500	16.91	−4.55	4.04	17965.16	1787.61	500	19.12	−5.47	4.01	17840.33	1803.59
1000	16.91	−4.55	4.04	17965.16	2482.01	1000	19.12	−5.47	4.01	17840.33	2713.18

Table 10
specific parameters of DMS-PSO optimization.

Case	Heat treatment	Not heat-treated
Population m	1350	1350
Number of data points in the sample set	1350	1350
The maximum number of iterations Nc_{max}	1000	1000
Final value of cost function L_{min}	17965.16	17840.33
Reference factor L_{min}/m	13.308	13.215
Parameter a_0 optimal solution	16.91	19.12
Parameter a_1 optimal solution	−4.55	−5.47
Parameter β optimal solution	4.04	4.01

4.2. Optimization of Weibull's parameters based on DMS-PSO algorithm

4.2.1. Particle swarm optimization

Because of the fewer parameters and fast convergence in model optimization, DMS-PSO is applied in parameter optimization in three-parameter Weibull distribution model. The Particle swarm optimization (PSO) algorithm was first proposed in 1995 [49]. The algorithm simulates the process of birds foraging and fish predation, which obtains the optimal solution to the problem through group collaboration. [50] The schematic diagram of finding the optimal solution in two-dimensional is shown in Fig. 7. And the dimension of the particle represents the number of parameters to be optimized for the problem v_{ix} and v_{iy} are the flying speed of the particle in the x and y directions, respectively.

The objective function of this study is MLE, and the solution to calculate the optimal parameters a_0, a_1 and β is a three-dimensional

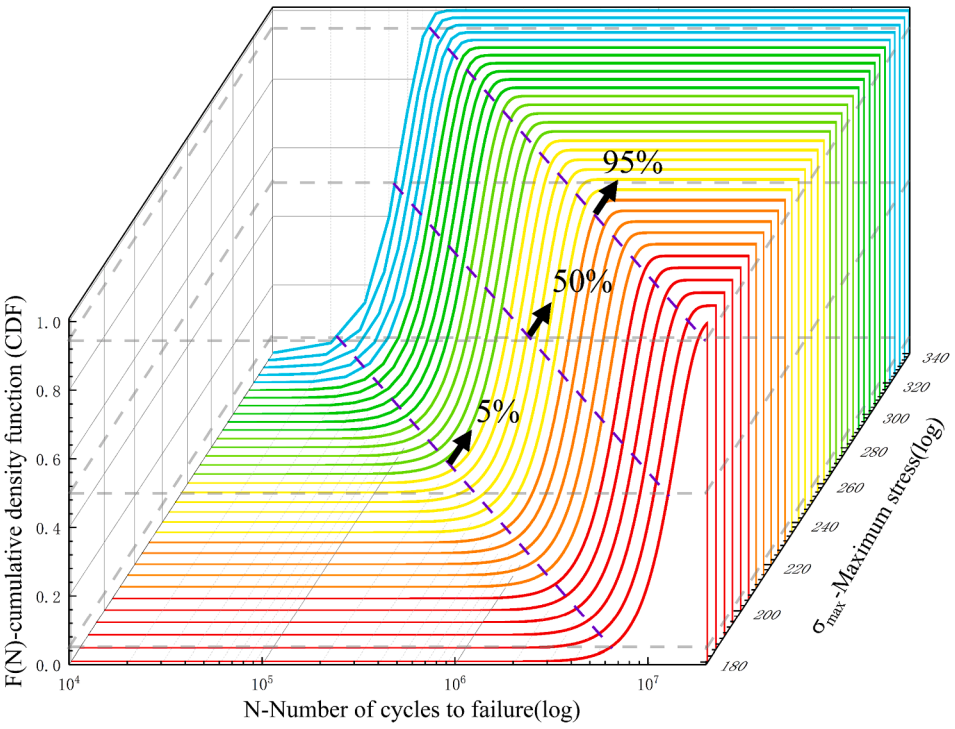

Fig. 17. CDF of different fatigue rupture probability (5%, 50% and 95%).

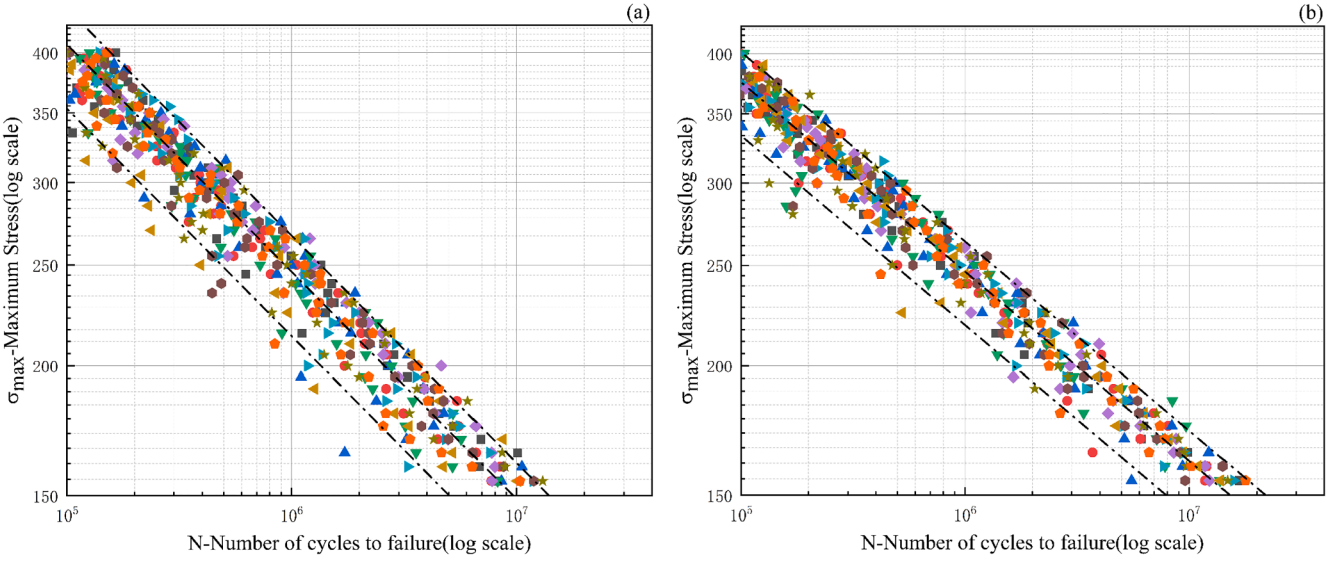

Fig. 18. S-N curve estimating by DMS-PSO for simulated sample sets: (a) heat treatment; (b) not heat-treated.

optimization process. In global optimization, the conditions for ending updating of particles can be as follows: the maximum number of iterations; the global optimal value remains unchanged for successive generations; and the objective function value is less than the setting accuracy ε. In traditional PSO algorithm, two iterative positions are recorded with the randomly distributed initial position: the historical optimal position of each particle $pBest^k$, and the global optimal position of the whole particle swarm $gBest^k$, as shown in Eq. (8).

$$\begin{cases} v_{id}^{k+1} = v_{id}^{k} + c_1 \cdot r_1 \cdot (pBest_{id}^{k} - x_{id}^{k}) + c_2 \cdot r_2 \cdot (gBest_{id}^{k} - x_{id}^{k}) \\ x_{id}^{k+1} = x_{id}^{k} + v_{id}^{k+1} \end{cases} \tag{8}$$

where v_{id}^k and x_{id}^k are the velocity and position of particle i in the k-th iteration respectively; ω is the inertia weight coefficient; c_1 and c_2 are local learning factors and global learning factors respectively. r_1 and r_2 are random numbers between [0,1]. In conventional particle swarm optimization, ω is set as linearly decreasing values: $\omega_{max} = 0$, $\omega_{min} = 0.2$, See Eq. (9); c_1 and c_2 are defined asynchronously and dynamically, as shown in Eq. (10), which expand the search scope to the global optimizing.

$$w = w_{max} - (w_{max} - w_{min}) \frac{k}{Nc_{max}} \tag{9}$$

$$\begin{cases} c_1 = c_{1,max} - (c_{1,max} - c_{1,min}) \dfrac{k}{Nc_{max}} \\ c_2 = c_{2,max} - (c_{2,max} - c_{2,min}) \dfrac{k}{Nc_{max}} \end{cases} \tag{10}$$

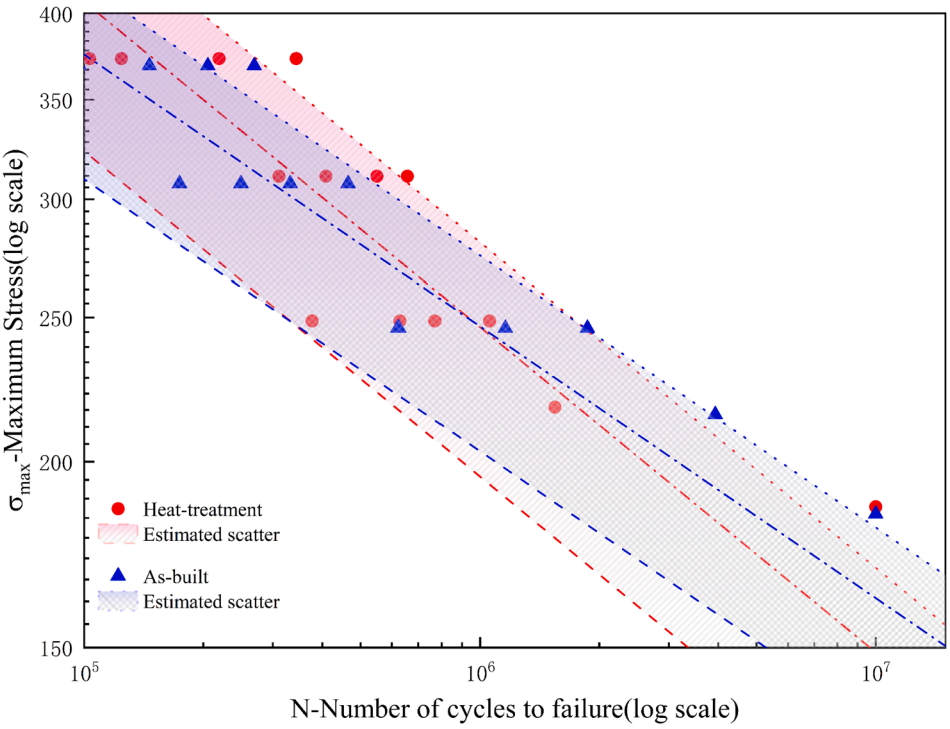

Fig. 19. Comparison of experimental data with estimated scatter.

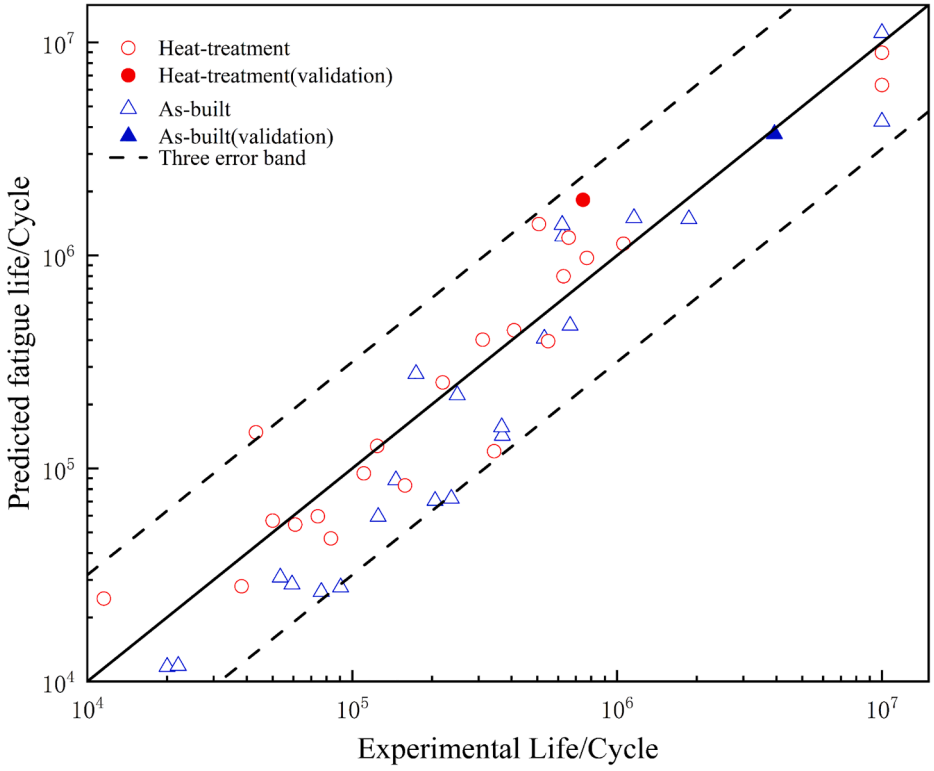

Fig. 20. Comparison between DMS-PSO results and experimental data.

where k is the number of iterations; Nc_{max} is the maximum number of iterations; $c_{1,max} = c_{2,max} = 2.5$, $c_{1,min} = c_{2,min} = 0.5$.

However, the PSO algorithm with the global variant also has the problem of local optima. And one of the solutions is to improve the local search ability by minimizing neighborhoods [51]. Liang JJ [47] designed Dynamic multi-swarm Particle swarm Optimization (DMS-PSO), which used a small Particle swarm to solve complex problems and dynamically recombined small Particle swarm so that the particles can exchange information among different populations and improve the exploration accuracy. In DMS-PSO, the whole particle swarm is separated into several small sub-particle swarms, and each sub-particle swarm is optimized as an independent population. Then, at a certain

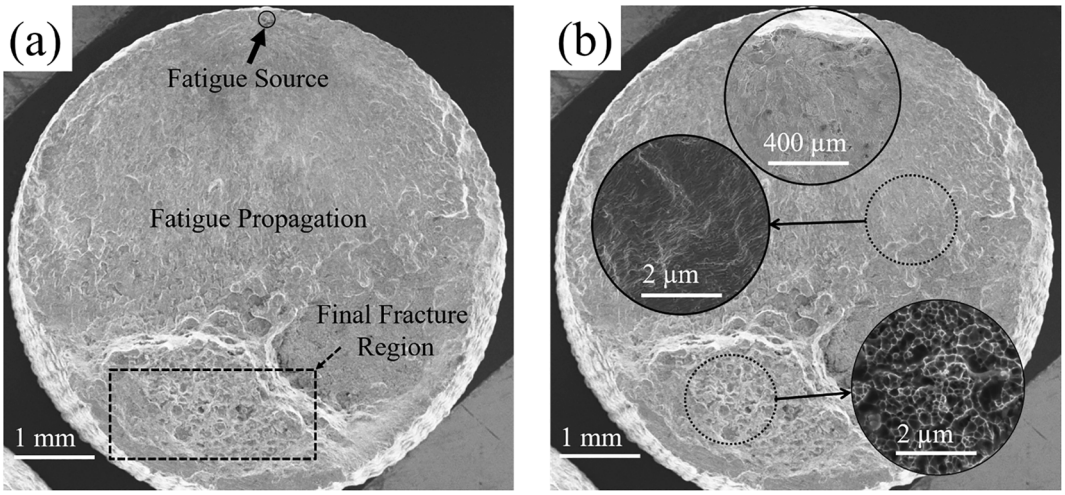

Fig. 21. Fracture morphology of fatigue specimen A-05: (a) Fracture diagram; (b) Microscopic morphology of each area.

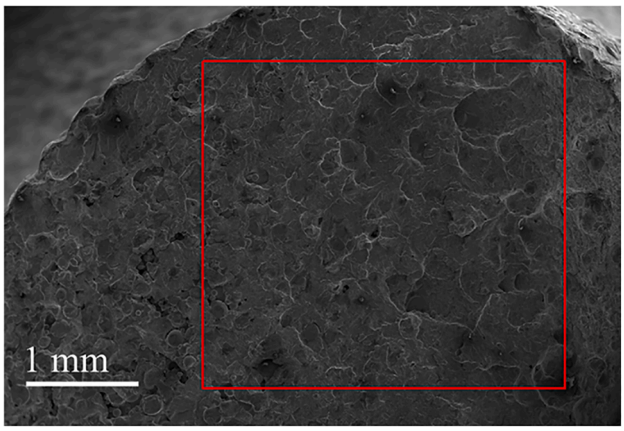

Fig. 22. EDS scan area.

Table 11
X-ray analysis.

Element	Atomic %	Conc %	Units	MDL
Si	3.750	1.874	wt.%	0.186
Cr	18.833	17.425	wt.%	0.820
Fe	60.900	60.518	wt.%	2.070
Ni	12.090	12.627	wt.%	1.148
Mo	4.426	7.555	wt.%	0.602

recombination period P, the whole particle swarm is randomly recombined again and the particle position is updated, as shown in Eq. (11). $sgBest_{id}^{k}$ is the global optimal value of each sub-particle swarm.

$$\begin{cases} v_{id}^{k+1} = w \cdot v_{id}^{k} + c_1 \cdot r_1 (pBest_{id}^{k} - x_{id}^{k}) + c_2 \cdot r_2 (sgBest_{id}^{k} - x_{id}^{k}) \\ x_{id}^{k+1} = x_{id}^{k} + v_{id}^{k+1} \end{cases} \tag{11}$$

The specific steps of DMS-PSO are shown in Fig. 8:

4.2.2. Fatigue S-N curve estimating based on DMS-PSO

In the Weibull parameter optimization of this study, the optimization results of the DMS-PSO and DASA algorithms were compared. The data were obtained from 65 fracture tests of S420MC in the study of Klemenc J [31], as shown in Table 4. In addition, the optimization termination condition in DMS-PSO is set to reach the maximum number of iterations, because the number of particles in PSO cannot be completely equivalent to the number of ant colonies in DASA. And it is hard to define whether the final PSO convergence is global when the termination condition is accuracy ε. Compared with DASA, the advantages of DMS-PSO are mainly embodied in search speed and data processing. The total calculation of 40,000 iterations based on experimental data lasted 32.76 s. And it is found that the minimum MLE value of the two algorithms has a slight difference on the premise of control variables. The MLE value of DMS-PSO is slightly smaller than that of DASA about 0.00112%, while the varies of a_0, a_1 and β are −0.488%, 0.632% and −0.288% respectively, as shown in Table 5. The difference was very small after repeated confirmation.

When constructing the sample set, the virtual sample set formed by the bootstrap procedure was divided into two subsets according to the stress size. The training set of 500 data points was also divided into two parts, and the data of each part were randomly selected from the two subsets of the bootstrap procedure [52]. Fig. 9 shows the discrete distribution of test data in the S-N domain, and Fig. 10 shows the discrete distribution of 500 virtual data in the S-N domain. For a specific mathematical model MLE, the effects of maximum iterations $Nc_{\max}$ on a_0, a_1 and β of the PSO algorithm necessitate analysis. Fig. 11 shows the influence of the maximum number of iterations on the results. When the maximum number of iterations is 1000, the values of the three parameters are determined, and the objective function value achieves the minimum. Because of the population recombination of DMS-PSO, the position updates of all particles have been completed. Since more population number m indicates more optimizer and better search capability, the number of particles is set as 500 in the DMS-PSO algorithm. Fig. 12 shows the comparison between the predicted data and the test data of S420MC steel. The predicted data are all in the three error bands of estimated scatter, which proves that the MLE estimating method based on DMS-PSO is effective.

5. Results and discussion

5.1. Quasi-static mechanical properties

The mechanical properties of 316L stainless steel prepared by SLM were obtained by the quasi-static tensile test. And the stress–strain curve is shown in Fig. 13(a). The stress–strain curves of group A and group B have no obvious yield point. For the three curves of each group, it is found that the discreteness of the stress–strain curve in group A is slightly larger than that in group B. And the specimens in group A have higher ultimate stress, higher ductility, and lower yield strength generally.

The transverse and longitudinal strain curve is shown in Fig. 13(b),

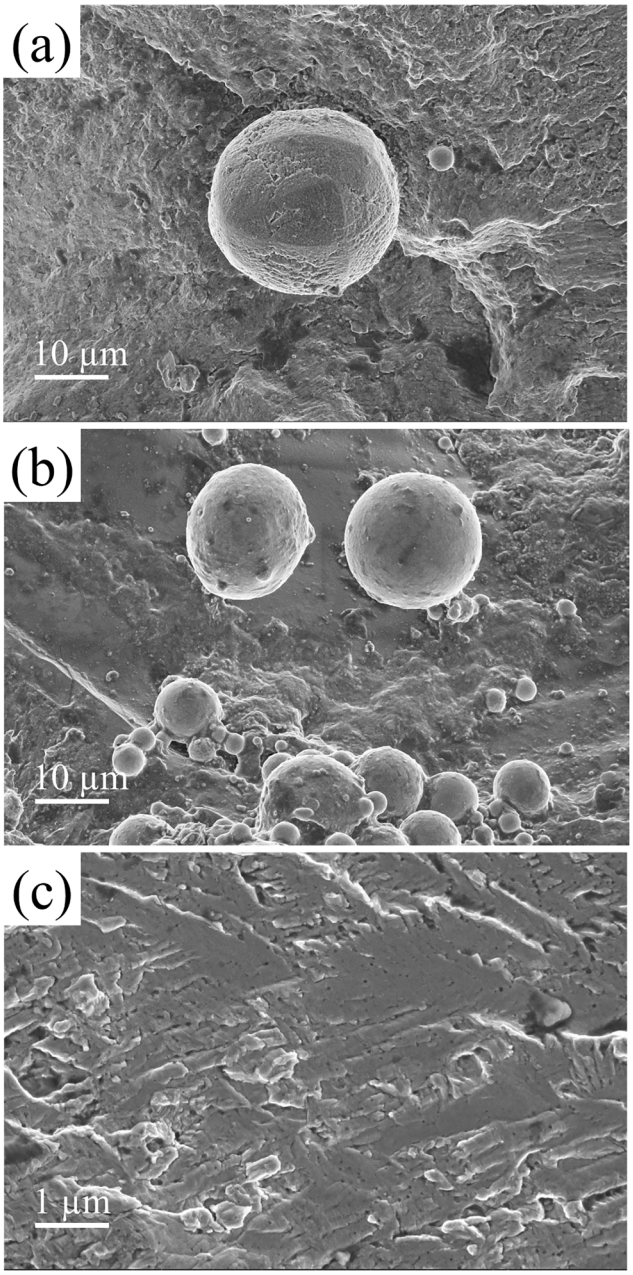

Fig. 23. Defects of fatigue fracture: (a) pores; (b) spherical region; (c) cracks propagation.

according to the standard GB/T 22315–2008 [53]. The Poisson's ratio is calculated by linear fitting. The ratio of transverse and longitudinal strain ε_x-ε_y is calculated by the least square method for linear fitting (slope of the line is Poisson's ratio). Within the range of 2000 axial strain in the elastic stage, the slope of group A which is equal to Poisson's ratio is generally larger. The specific data is shown in Table 6, and C.V in Table 6 means the coefficient of variation. For material reliability in this study, the yield strength and ultimate strength of 316L stainless steel prepared by SLM meet the production requirements of GB/T 3280–2015 [54]. The standard value of yield strength and ultimate strength of steel plate are 180 MPa and 485 MPa, and the standard value of elongation is 40%. For all specimens, the range of elastic modulus is 131.8 ~ 168.2 GPa; the range of Poisson's ratio is 0.2330 ~ 0.2930; the range of yield strength is 377.2 ~ 503.2 MPa; the range of tensile strength is 610.2 ~ 640.0 MPa; the range of elongation is 41.40%~47.20%; the range of area shrinkage is 35.00%~50.60%. In addition, the yield strength of heat-treated specimens is lower than that of unheated specimens, while the tensile strength, elastic modulus, and elongation are higher.

5.2. Fatigue life results

The fatigue data are shown in Fig. 14(a), while the fatigue life of both groups A and B are over 10^7 cycles at 30% stress level. According to the standard GB/T 24176–2009 [55], the logarithmic linear fitting S-N curve (σ_{max}-N, $\sigma_{max} = \sigma_m + \sigma_a$) is obtained by analyzing the S-N relationship with a linear mathematical model. For 7 heat-treated specimens at a high-stress level ($\sigma_m = 248.72$ MPa) are measured, the normalized deviation of the log-linear fitting is close to the normal distribution, as shown in Fig. 14(b). The logarithmic fitting equations of heat-treated specimens and unheated specimens are $lg(\sigma_{max}) = 3.8135–0.2366 \times lg(N)$ and $lg(\sigma_{max}) = 3.6394–0.2043 \times lg(N)$, Where R^2 is 0.8697 and 0.8343, respectively.

All the fatigue data points are sorted out and combined with the existing data in an article [56], as shown in Fig. 15 including the two processes in the test and the two processes (mechanical polishing and as-built) in the article. Fig. 14(a) shows that two life curves intersect at around $\sigma_{max} = 350$ MPa, and the improvement of fatigue life by heat treatment diminishes with the decreasing stress. However, the different discreteness under different stress is not well reflected in the fitting method. For these reasons, the S-N estimating model is introduced to predict the fatigue life and fit the S-N curve.

The objective function is set as the cost function MLE. In DMS-PSO optimization, the population m is selected as 10, the dimension n is 3, and the maximum number of iterations Nc_{max} is 1000. Before starting the iteration, the amplitude of a_0, a_1 and β is limit: $a_{0,max} = 50$; $a_{0,min} = 0$; $a_{1,max} = -1$; $a_{1,min} = -30$; $\beta_{max} = 20$; $\beta_{min} = 0.5$. According to the bootstrap procedure, a small amount of test data is expanded into data set $S=\{(\sigma_{max,i}, N_i); i = 1,2...,n\}$, the data set S is divided according to t increasing stress levels (180 ~ 400 MPa, $t = 45$). Meanwhile, n data are selected for the training set for optimization ($n = 45$, 90, 180, 450, 900, 1350). and the variations of the final cost function under different virtual sample sets were observed. In the optimization, the variable $P=(x_1, x_2, x_3)=(a_0, a_1, \beta)$, and the initial shape parameter β is set as $\beta = 4$. The initial values of a_0 and a_1 are estimated by linear regression of $\sigma_{max,i}$ and N_i in the data of sample set S, as shown in Eq. (10). Table 7 and Table 8 show the three-parameter optimization results of heat-treated and unheated 316L prepared by SLM respectively.

$$\begin{bmatrix} a_0^{sr=0} \\ a_1^{sr=0} \end{bmatrix} = (X^T \cdot X)^{-1} \cdot X^T \cdot Y; X = \begin{bmatrix} 1 & \log(\sigma_{max}, 1) \\ & \vdots \\ 1 & \log(\sigma_{max}, n) \end{bmatrix}_{n\times 2}, Y = \begin{bmatrix} \log(N_1) \\ \vdots \\ \log(N_n) \end{bmatrix}_{n\times 1} \tag{10}$$

In Table 7 and Table 8, different sample sets correspond to different final values of parameters a_0, a_1 and β. With larger sample set, better description of the probabilistic distribution of fatigue data can be achieved. Since the cost function results with little difference, the parameter with more data points n in the sample set is preferentially selected, because it is more representative.

For the sample set of 1350 data points, it is found that after 1000 times, the iteration result had maintained global convergence, the value of L_{min}/m remained unchanged in the optimization process, and the cost function converged to the minimum value. The values of the stable parameters are shown in Fig. 16, and the specific results of the iteration are shown in Table 9. All algorithm calculations in this article are carried out on an HP desktop computer with the Intel(R) Core (TM) I7-9700 CPU processor and memory capacity of 8.00 GB. Procedure code development is realized in MATLAB software.

DMS-PSO optimization in large sample sets is feasible and fast. Compared with DASA [57], the feasibility of PSO optimization in this application is embodied as follows: 1) A large number of populations cost less time, when the optimal values of a_0, a_1 and β in MLE were

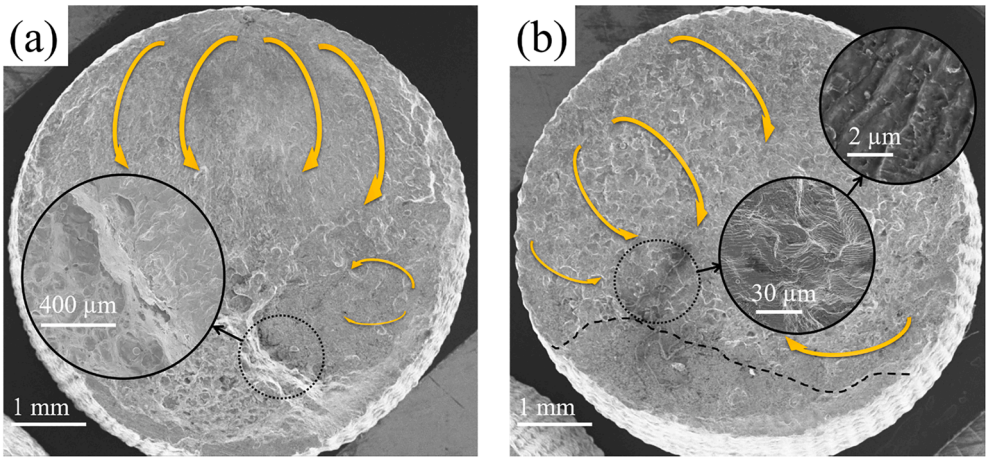

Fig. 24. Crack initiation and cracks propagation: (a) fatigue specimen A-05; (b) fatigue specimen A-011.

searched. 2) DMS-PSO always converges to the global optimal value of the cost function, but DASA occasionally converges to the local optimal value[36]. Specific DMS-PSO optimization parameters are shown in Table 10:

Finally, the optimal solutions of a_0, a_1 and β are substituted into Eq. (8) to obtain the cumulative density function (CDF). According to Eq. (9), the estimated scatter of arbitrary fracture probability y can be obtained, as shown in Fig. 17. According to Eq. (4), the specific Weibull distribution mathematical model is established. Fig. 18(a) and Fig. 18(b) are the fatigue life discrete band of the simulated S-N curve after HIP and without heat treatment relatively. Different patterns represent 10 groups of 50 fatigue test data. The dotted lines in Fig. 19 represent the boundaries of 95%, 50%, and 5% of rupture probability from top to bottom.

Compared with the experimental data, most experimental data are distributed in the estimated scatter, as shown in Fig. 19. Two test data of specimens (A-06 and B-06) are imported into the estimating model for secondary verification, and the results showed that they were all in the three error bands of the prediction model, as shown in Fig. 20. In general, the high cycle fatigue life of heat-treated specimens is longer than that of specimens not heat-treated. However, the S-N curves of the two treatments intersect at around the point (250 MPa, 10^6), which means that the HIP treatment can improve fatigue life at relatively high stresses ($\sigma_{max} > 250$ MPa), but has little help in low stresses. It is related to the fatigue response with different yield strengths and ductility values [58]. Materials with higher yield strength perform better in low-stress fatigue, while ductility predominantly governs the fatigue life under higher stresses. Therefore, the HIP treatment can be beneficial in high-stress conditions. Moreover, the failure probability and the life scatters of the material can be an indication of finite life design. Therefore, the Weibull model based on DMS-PSO algorithm is capable of depicting probabilistic S-N curves for the endurance limit of each stress. SLM316L in this study has little probability for fracture under 1000,000 cycles at 200 MPa, around 32% percent of the ultimate tensile strength.

5.3. Fatigue fracture

The influencing factors of the predicted fatigue performance were analyzed by fracture metallography. Fig. 21 shows the overall morphology of the fatigue fracture of the No. 5 specimen in group A ($\sigma_{max} = 248.72$ MPa, $N = 769865$). The fatigue fracture is composed of three regions: the fatigue source, the crack propagation region, and the final fracture region. Fig. 21(a) is the region diagram of the fatigue fracture. The fracture cracks are first generated from the fatigue source. Then the cracks extend to the final instantaneous fracture region, resulting in the overall fracture. In this process, the crack in the fatigue growth region is similar to the brittle fracture, while the rupture in the final instantaneous fracture region is similar to the plastic fracture. Therefore, the micromorphology of the propagation region is mostly a stepped cleavage morphology. In contrast, the micromorphology of the final fracture region is mostly a denser dimple morphology. The specific fracture morphology is shown in Fig. 21(b).

The energy-dispersive X-ray spectroscopic (EDS) observation area of the fracture morphology of the No. 5 specimen is shown in Fig. 22. Based on the local chemical analysis of the dimple area in Table 11, it can be concluded that the element composition of the dimple structure with severe fracture does not deviate significantly from that of 316L powder material.

In the process of SLM preparation, the high-speed melting and solidification of the powder make part of the powder insufficiently melted, which is called incomplete melting in the molten pool (unfused region). The connection between adjacent deposition layers is insufficient in this area, resulting in larger internal gaps, cracks, and delamination. And the spherical defects in the propagation region are mostly pore defects, which are mostly caused by insufficient cooling and gas escaping during condensation. These defects are always stress-concentrated areas in fatigue cracks, which necessitate observation in detail. Fig. 23(a) shows the pores of the fatigue fracture of the No. 11 specimen in group A ($\sigma_{max} = 248.72$ MPa, $N = 377096$). Compared with the No. 5 specimen ($\sigma_{max} = 248.72$ MPa, $N = 769865$) of the same level of stress, the fatigue life of the two is several times different. The pore size shown in the figure is 20 $\sim$ 25 μm, which is widely existed in the fracture of the No. 6 specimen. As shown in Fig. 23(b), the spherical region formed by continuous pore defects has a destructive effect on fatigue life. Fig. 23(c) shows the cracks propagation region before the rupture.

The fatigue failure process can be well described by the crack initiation and cracks propagation. In this study, Multiple cracks were initiated from the small notch on the surface, which is consistent with previous studies [14]. Fig. 24(a) illustrates the directions of crack propagation in No. 5 specimen ($\sigma_{max} = 248.72$ MPa, $N = 769865$), which starts from two main crack sources. But the rupture of the No. 11 specimen in group A ($\sigma_{max} = 248.72$ MPa, $N = 377096$) was originated from a large group of crack sources, while the crack propagation is characterized by a radial flow pattern towards the core. The microstructure of the multidirectional cracks propagation, as shown in Fig. 24 (b), was characterized by a pattern of ripples called striations, which represent the crack condition under each fatigue load cycle. Multi-cracks led to a large drop height perpendicular to the fracture surface, while the overall fatigue life is shortened by the smaller final fracture region. Moreover, the dimples morphology in No. 11 specimen in group A ($\sigma_{max} = 248.72$ MPa, $N = 377096$) was relatively flat. Therefore, the generation of multiple fatigue sources may be the reason for the deviation of

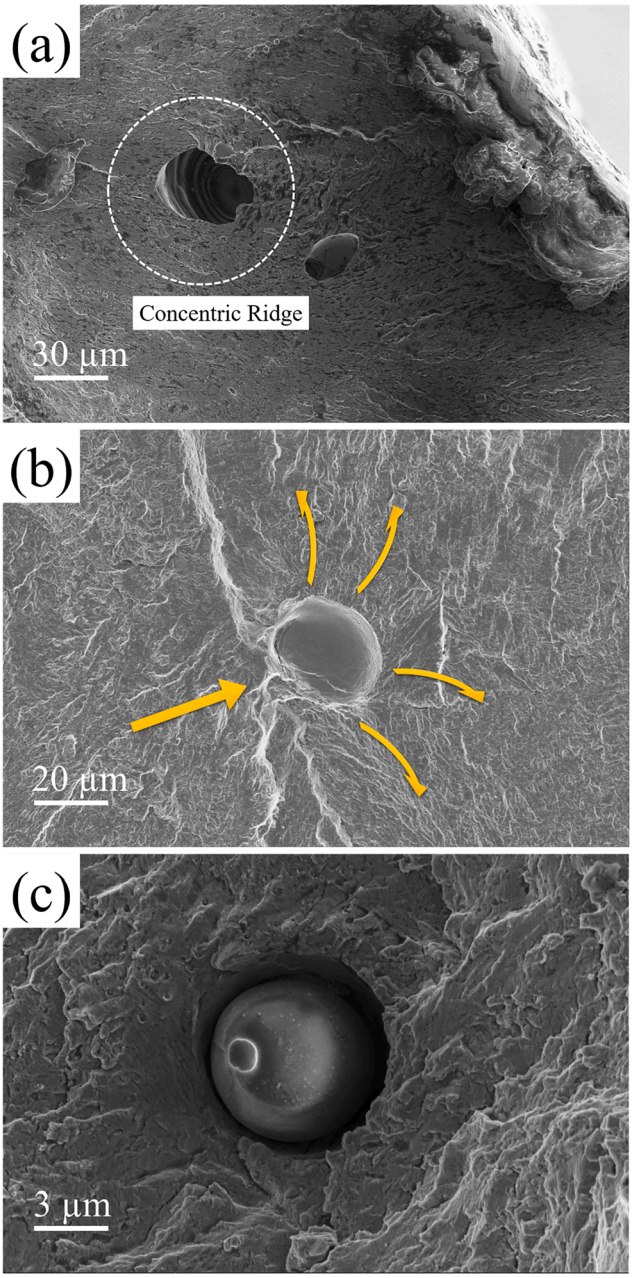

Fig. 25. Defects in crack propagation: (a) concentric bridge; (b) the direction of crack propagation; (c) powder.

fatigue data.

The generation of crack sources in AM materials is influenced not only by the edge surface, but also by the invisible defects inside the materials. For example, concentric bridges closed to the edge will increase the possibility of crack initiation, as shown in Fig. 25(a). And the pores created by gas entrapment will change the direction of crack propagation, as shown in Fig. 25(b). Fig. 25(c) displays an un-melted powder in the No. 3 specimen in group B (σ_{max} = 368.88 MPa, N = 146229), resulting from the incomplete re-melting of the previous layer [59].

The effect of HIP treatment on fatigue performance was analyzed qualitatively by observing the morphology of fracture regions under polishing for all specimens in this study. For the specimens constructed vertically, the columnar grains of the long axis were stretched in the propagation region, where existed a large number of cleavage steps. Fig. 26(a) and Fig. 26(b) are cleavage steps of No. 4 specimen in group A (σ_{max} = 310.9 MPa, N = 550005) and No. 4 specimen in group B (σ_{max} = 307.4 MPa, N = 249220) respectively. The columnar grains after HIP are finer, with higher drop height in load direction. It indicates that the grains are stretched more intensely and fully, which may be attributed to the high plasticity after HIP treatment. Influenced by the range and depth of crack propagation, secondary cracks often appear when cracks grow into striations, with the consumption of propagation energy and reduction of crack propagation rate. Therefore, the fatigue life after HIP treatment is improved.

when the specimens cannot resist cyclic loading, they fracture immediately from the unstable crack propagation. Fig. 27(a) is the microscopic morphology of the fracture dimples of the No. 1 specimen in group A (σ_{max} = 497.44 MPa, N = 11545), and Fig. 27(b) is the morphology of the fracture dimples of the No. 1 specimen in group B (σ_{max} = 491.84 MPa, N = 22051). In the case of low-cycle and high-stress levels, the fracture of the specimens in the final rupture regions is close to a quasi-static fracture which endured sufficient plastic deformation with large and deep dimples. In the study, It was found that the dimples of the No. 1 specimen in group A are smaller and denser than those of the No. 11 specimen in group B. According to the difference of surface morphology and molten layer, group A releases more internal residual stress in the process than group B, resulting in smaller crystal grains and melting gaps.

Fig. 28(a) shows the microscopic morphology of the fracture dimples of the No. 6 specimen in group A under high-cycle fatigue (σ_{max} = 217.63 MPa, N = 1544911), and Fig. 28(b) shows the dimples of the No. 6 specimen in group B (σ_{max} = 215.18 MPa, N = 3929614). The two figures show that the overall fracture dimples under high-cycle low-stress cycles are small. Such fracture is typical for low-stress intensity factors when the cyclic stress is lower than the yield point of the material. However, it was found that the dimples of group B were smaller than group A at this time, which is different from the low-cycle and high-stress situation. After scanning the fractures of other high-cycle fatigue specimens, the microscopic morphology of the fracture dimples of the

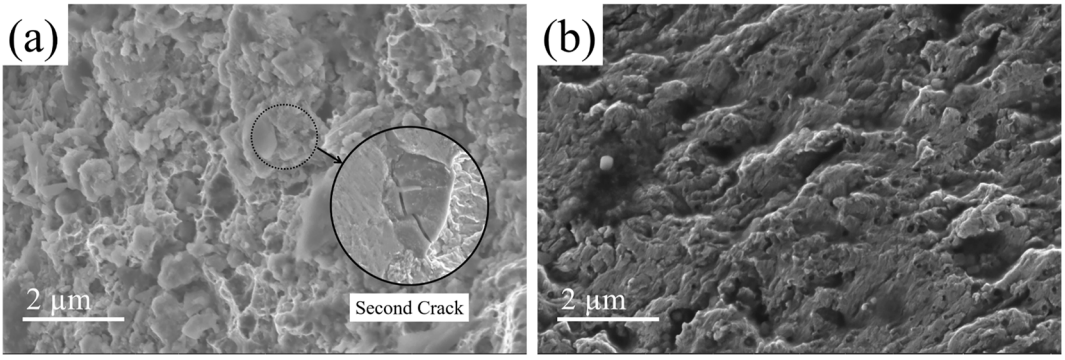

Fig. 26. Cleavage steps: (a) fatigue specimen A-04; (b) fatigue specimen B-04.

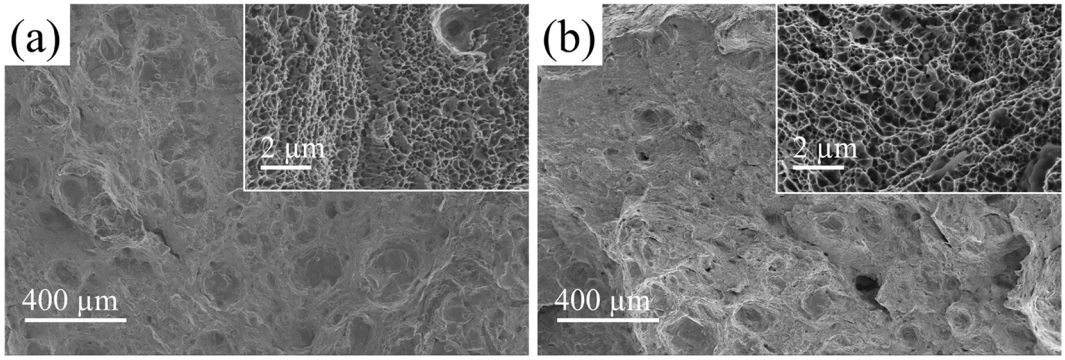

Fig. 27. Comparison of low-cycle fatigue fracture dimples: (a) fatigue specimen A-01; (b) fatigue specimen B-01.

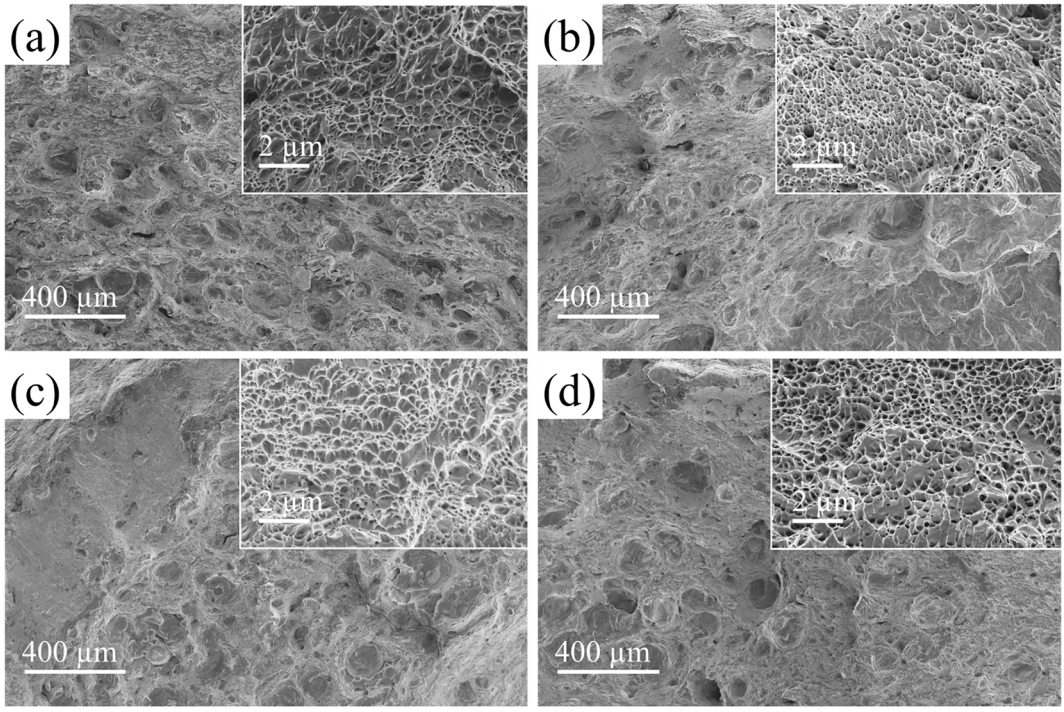

Fig. 28. Comparison of high-cycle fatigue fracture dimples: (a) fatigue specimen A-06 (b) fatigue specimen B-06; (c) fatigue specimen A-05; (d) fatigue specimen B-05.

No. 5 specimen in group A ($\sigma_{max} = 248.72$ MPa, $N = 769865$) as shown in Fig. 28(c). Fig. 28(d) is the morphology of the fracture dimples of the No. 5 specimen in group B ($\sigma_{max} = 245.92$ MPa, $N = 1158335$). The dimples of group B showed smaller fineness and more irregular surface than group A. When observing the morphology with a larger magnification, the dimple fracture of group B is stepped fluctuating, while the dimple fracture of group A is relatively flat. It shows that the final rupture region of group B has experienced a severe rupture. The fatigue life under low stress is related to crack propagation. However, a severe fracture means a shorter response time from crack propagation to final rupture. As a result, this phenomenon is consistent with the longer life of group B than group A in crack propagation of the high-cycle fatigue, with the better performance of the quasi-static properties of yield strength.

6. Conclusion

The study focuses on the fatigue performance of 316L stainless steel manufactured by SLM under HIP heat-treatment. And the three-parameter Weibull distribution model is applied to obtain the S-N curves and fatigue life scatters, in which the DMS-PSO algorithm is first introduced to optimize the parameters of the model. The DMS-PSO algorithm can always get the optimal value in the parameter estimating in Weibull model of various sample sets for self-adaptation with efficiency, ease of use, and simplicity of implementation. The effectiveness of the fatigue life prediction based on three-parameter Weibull distribution model optimized by the DMS-PSO algorithm is proved by comparison with that by the existing DASA algorithm. The MLE value of DMS-PSO is slightly smaller than that of DASA about 0.00112%, while the varies of a_0, a_1 and β are −0.488%, 0.632% and −0.288% respectively. And the results show DMS-PSO algorithm can avoid the local optimal solutions and achieve faster convergence. When fatigue life prediction based on the model by DMS-PSO algorithm was applied in the fatigue-life curves estimation of SLM316L, the S-N curves were highly consistent with the metallographic and fractographic phenomena.

For SLM316L, the HIP process can homogenize the microstructure and reduce negative influences by the defects (unfused regions, spherical regions, and pores), which is explained by the metallographic structure of the fatigue fracture with the consistent roughness surface. And the crack initiation often starts at the internal defects caused by the

laser melting process. Moreover, HIP heat-treatment contributes to a reduction of about 22% percent in the yield strength (from 500.1 MPa to 392.2 MPa in this study), and an increase in the ductility and elastic modulus of the material by around 10% percent. The S-N curve estimation exhibits that the HIP heat-treatment improved the fatigue life of specimens at high stresses ($\sigma_{max} > 250$ MPa), while the as-built state is enough for lower stress applications. The visible stabilization of high-stress fatigue life brought by HIP treatment is still the main advantage in post-treatments of SLM technology.

The authors declare that they have no known competing financial interests or personal relationships that could have appeared to influence the work reported in this paper.

Declaration of Competing Interest

The authors declare that they have no known competing financial interests or personal relationships that could have appeared to influence the work reported in this paper.

Acknowledgments

The authors sincerely acknowledge the support from the Science and Technology Project of Quanzhou, China (No.2019STS01) and the Collaborative Innovation Platform Project of the Fuxiaquan National Independent Innovation Demonstration Zone, China (No.2020FX01).

References

[1] Santos EC, Shiomi M, Osakada K, et al. Rapid manufacturing of metal components by laser forming. Int J Mach T M 2006;46(12–13):1459–68.
[2] Brandl E, Heckenberger U, Holzinger V, et al. Additive manufactured AlSi10Mg samples using Selective Laser Melting (SLM): Microstructure, high cycle fatigue, and fracture behavior. Mater Eng 2012;34:159–69.
[3] Tolosa I, Garciandía F, Zubiri F, et al. Study of mechanical properties of AISI 316 stainless steel processed by "selective laser melting", following different manufacturing strategies. Int J AM Tech 2010;51(5):639–47.
[4] Mower TM, Long MJ. Mechanical behavior of additive manufactured, powder-bed laser-fused materials. Mater Sci Eng A 2016;651:198–213.
[5] Montero-Sistiaga ML, Godino-Martinez M, Boschmans K, et al. Microstructure evolution of 316L produced by HP-SLM (high power selective laser melting). Addit Manuf 2018;23:402–10.
[6] Suryawanshi J, Prashanth K, Ramamurty U. Mechanical behavior of selective laser melted 316L stainless steel. Mater Sci Eng A 2017;696:113–21.
[7] Cherry JA, Davies HM, Mehmood S, et al. Investigation into the effect of process parameters on microstructural and physical properties of 316L stainless steel parts by selective laser melting. Int J AM Tech 2015;76(5–8):869–79.
[8] Ziółkowski G, Chlebus E, Szymczyk P, et al. Application of X-ray CT method for discontinuity and porosity detection in 316L stainless steel parts produced with SLM technology. Arch Civil and Mech Eng 2014;14(4):608–14.
[9] Löber L, Flache C, Petters R, et al. Comparison of different post processing technologies for SLM generated 316l steel parts. Rap Pro J 2013.
[10] Montero Sistiaga M, Nardone S, Hautfenne C, et al. Effect of heat treatment of 316L stainless steel produced by selective laser melting (SLM). In: in: Proceedings of the 27th Annual International Solid Freeform Fabrication Symposium-An Additive Manufacturing Conference. Solid Freeform Fabrication; 2016. p. 558–65.
[11] Kong DC, Dong CF, Ni XQ, et al. Mechanical properties and corrosion behavior of selective laser melted 316L stainless steel after different heat treatment processes. Mater Sci Technol 2019;35(7):1499–507.
[12] Leuders S, Lieneke T, Lammers S, et al. On the fatigue properties of metals manufactured by selective laser melting—The role of ductility. J Mater Res 2014;29(17):1911–9.
[13] Riemer A, Leuders S, Thöne M, et al. On the fatigue crack growth behavior in 316L stainless steel manufactured by selective laser melting. Eng Frac Mech 2014;120:15–25.
[14] Elangeswaran C, Cutolo A, Muralidharan GK, et al. Effect of post-treatments on the fatigue behaviour of 316L stainless steel manufactured by laser powder bed fusion. Int J Fatigue 2019;123:31–9.
[15] Zur Schütz W, der Schwingfestigkeit Geschichte. Materialwiss Werkstofftech 1993;24(6):203–32.
[16] Wöhler A. Über die festigkeitsversuche mit eisen und stahl. Ernst & Korn 1870.
[17] Kastratović G, Vidanović N, Grbović A, et al. Approximate determination of stress intensity factor for multiple surface cracks. FME transactions 2018;46(1):39–45.
[18] Grbovic A, Rasuo B. FEM based fatigue crack growth predictions for spar of light aircraft under variable amplitude loading. Eng Fail Anal 2012;26:50–64.
[19] Grbovic A, Rasuo B. Chapter 2: Use of Modern Numerical Methods for Fatigue Life Predictions. In: Recent Trends in Fatigue Design. New York: Nova Science Publishers; 2014. p. 31–74.
[20] Liu Y. Stochastic modeling of multiaxial fatigue and fracture. Vanderbilt University; 2006.
[21] Liakat M, Khonsari MM. An experimental approach to estimate damage and remaining life of metals under uniaxial fatigue loading. Materials Design 2014;57:289–97.
[22] Miner MA. Cumulative damage in fatigue. Applied Mech 1945;12:A159-A164.
[23] Palmgren A. Die Lebensdauer von Kugellagern (Life Length of Roller Bearings. In German). Zeitschrift des Vereines Deutscher Ingenieure 1924;(0341-7258).
[24] Xiong JJ, Shenoi RA, Fatigue and fracture reliability engineering, Springer Science & Business Media, 2011.
[25] Zhang M, Sun C-N, Zhang X, et al. Fatigue and fracture behaviour of laser powder bed fusion stainless steel 316L: Influence of processing parameters. Mater Sci Eng, A 2017;703:251–61.
[26] Nelson W. Fitting of fatigue curves with nonconstant standard deviation to data with runouts. Journal of Testing Evaluation 1984;12(2):69–77.
[27] Rinne H. The Weibull distribution: a handbook. Chapman and Hall/CRC; 2008.
[28] Caiza PDT, Ummenhofer T. A probabilistic Stüssi function for modelling the SN curves and its application on specimens made of steel S355J2+ N. Int J Fatigue 2018;117:121–34.
[29] Castillo E, Ramos A, Koller R, et al. A critical comparison of two models for assessment of fatigue data. Int J Fatigue 2008;30(1):45–57.
[30] Schijve J. Statistical distribution functions and fatigue of structures. Int J Fatigue 2005;27(9):1031–9.
[31] Klemenc J, Fajdiga M. Estimating S-N curves and their scatter using a differential ant-stigmergy algorithm. Int J Fatigue 2012;43:90–7.
[32] Strzelecki P. Determination of fatigue life for low probability of failure for different stress levels using 3-parameter Weibull distribution. Int J Fatigue 2021;145.
[33] Shen HW, Lin JZ, Mu ES. Probabilistic model on stochastic fatigue damage. Int J Fatigue 2000;22(7):569–72.
[34] Liang J-J, Suganthan PN. Dynamic multi-swarm particle swarm optimizer, in: Proceedings 2005 IEEE Swarm Intelligence Symposium, 2005. SIS 2005. IEEE, 2005; pp. 124-129.
[35] Liverani E, Toschi S, Ceschini L, et al. Effect of selective laser melting (SLM) process parameters on microstructure and mechanical properties of 316L austenitic stainless steel. J Mater Processing Tech 2017;249:255–63.
[36] Glodež S, Klemenc J, Zupanič F, et al. High-cycle fatigue and fracture behaviours of SLM AlSi10Mg alloy. Transactions of Nonferrous Metals Society of China 2020;30(10):2577-2589.
[37] Guo C, Lin F, Ge WJ. Study on selective melting of 316L stainless steel by electron beam[J]. Chinese Journal of mechanical engineering. Mech Eng 2014;50(21):152–8.
[38] Jiang HZ, Li ZY, Feng T, et al. Effect of Process Parameters on Defects, Melt Pool Shape, Microstructure, and Tensile Behavior of 316L Stainless Steel Produced by Selective Laser Melting. J Acta Metallurgica Sinica 2021;34(4):495–510.
[39] GB. Gb/t228.1-2010. Metallic materials - Tensile testing - Part 1 : Method of test at room temperature. Ministry of Housing and Urban-Rural Development of the People's Republic of China 2010.
[40] GB. Gb/t3075-2008. Metallic materials - Fatigue testing - Axial-force-controlled method. Ministry of Housing and Urban-Rural Development of the People's Republic of China 2008.
[41] Zhou YC, Zhao Y. Tensile properties of 316L stainless steel prepared by additive manufacturing technology. Chin Civil ENG J 2020;53(10):26–35.
[42] Elangeswaran C, Cutolo A, Muralidharan GK, et al. Effect of post-treatments on the fatigue behaviour of 316L stainless steel manufactured by laser powder bed fusion. Int J Fatigue 2019;123:31–9.
[43] Uhlmann E, Fleck C, Gerlitzky G, et al. Dynamical fatigue behavior of additive manufactured products for a fundamental life cycle approach. Procedia CIRP 2017;61:588–93.
[44] Solberg K, Berto F. What is going on with fatigue of additively manufactured metals? Mater Des Process Commun 2019;1(5).
[45] Cizman J, Fajdiga M. Load carrying capacity analysis of materials for aluminum rims. Str Ves-J Mech Eng 1999;45(11):412–22.
[46] Pascual FG, Meeker WQ. Estimating fatigue curves with the random fatigue-limit model. Technometrics 1999;41(4):277–89.
[47] Liang JJ, Suganthan PN. Dynamic multi-swarm particle swarm optimizer, in: Proceedings 2005 IEEE Swarm Intelligence Symposium, 2005. SIS 2005. IEEE, 2005; pp. 124-129.
[48] Korošec P, Šilc J, Filipič B. The differential ant-stigmergy algorithm. Inf Sci 2012;192:82–97.
[49] Eberhart R, Kennedy J. Particle swarm optimization, in: Proceedings of the IEEE international conference on neural networks. Citeseer, 1995; pp. 1942-1948.
[50] Poli R, Kennedy J, Blackwell T. Particle swarm optimization. Swarm Intell 2007;1(1):33–57.
[51] Kennedy J. Small worlds and mega-minds: effects of neighborhood topology on particle swarm performance, in: Proceedings of the 1999 congress on evolutionary computation-CEC99 (Cat. No. 99TH8406). IEEE, 1999; pp. 1931-1938.
[52] Franklin J. The elements of statistical learning: data mining, inference and prediction. The Mathematical Intelligencer 2005;27(2):83–5.
[53] GB. Gb/t22315-2008. Metallic materials - Determination of modulus of elasticity and poisson's ratio. Ministry of Housing and Urban-Rural Development of the People's Republic of China 2008.
[54] GB. Gb/t3280-2015. Cold rolled stainless steel plate, sheet and strip. Ministry of Housing and Urban-Rural Development of the People's Republic of China 2015.
[55] GB. Gb/t24176-2009. Metallic materials - Fatigue testing - Statistical planning and analysis of data. Ministry of Housing and Urban-Rural Development of the People's Republic of China 2009.

[56] Spierings AB, Starr TL, Wegener K. Fatigue performance of additive manufactured metallic parts. Rap Pro J 2013.
[57] Klemenc J, Seruga D, Nagode M. A durability prediction for the magnesium alloy AZ31 based on plastic and total energy. Metals 2019;9(9):973.
[58] Manson S, Hirschberg M. The role of ductility, tensile strength and fracture toughness in fatigue. J Franklin Inst 1970;290(6):539–48.
[59] Qiu C, Adkins NJ, Attallah MM. Microstructure and tensile properties of selectively laser-melted and of HIPed laser-melted Ti–6Al–4V. Mater Sci Eng A 2013;578:230–9.